Available online at www.sciencedirect.com

ScienceDirect

journal homepage: www.elsevier.com/locate/he

X-ray CT-based numerical investigation of nickel foam-based GDLs under compression

Mustafa Ercelik [a,b], *Mohammed S. Ismail* [c], *Kevin J. Hughes* [a,*], *Derek B. Ingham* [a], *Lin Ma* [a], *Mohamed Pourkashanian* [a,d]

[a] *Energy 2050, Department of Mechanical Engineering, Faculty of Engineering, The University of Sheffield, Sheffield, S3 7RD, United Kingdom*

[b] *Department of Energy Systems Engineering, Faculty of Engineering and Natural Sciences, Iskenderun Technical University, 31200, Iskenderun, Hatay, Turkey*

[c] *School of Engineering, University of Hull, Hull HU6 7RX, United Kingdom*

[d] *Translational Energy Research Centre (TERC), University of Sheffield, Sheffield, S9 1ZA, United Kingdom*

HIGHLIGHTS

- Nickel foam was numerically evaluated as a potential GDL material for PEFCs.
- X-ray CT images, 3D-printed compression device and numerical models were employed.
- Structural and transport properties of nickel foam under compression were determined.
- Anisotropy of nickel foam permeability significantly increases with compression.
- Nickel foam has superior properties compared to conventional GDLs.

GRAPHICAL ABSTRACT

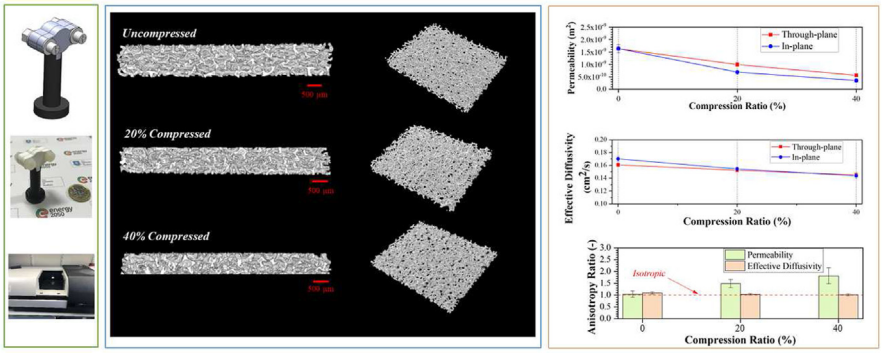

ARTICLE INFO

Article history:
Received 4 February 2023
Received in revised form
21 June 2023
Accepted 1 July 2023
Available online 20 July 2023

Keywords:
Polymer electrolyte fuel cell
Gas diffusion layer

ABSTRACT

Nickel foams feature superior structural and transport characteristics and are therefore strong candidates to be used as gas diffusion layers (GDLs) in polymer electrolyte fuel cells (PEFCs). In this work, the impact of compression on the key structural and transport properties has been investigated, including employing a specially designed compression apparatus and X-ray computed tomography. Namely, 20 equally spaced two-dimensional CT based images and numerical models have been used/developed to investigate the sensitivity of the key properties of nickel foams (porosity, tortuosity, pore size, ligament thickness, specific surface area, gas permeability and effective diffusivity) to realistic compressions normally experienced in PEFCs. Wherever applicable, the anisotropy in the property has been investigated. One of the notable findings is that, unlike porosity and

* *Corresponding author.*
E-mail address: k.j.hughes@sheffield.ac.uk (K.J. Hughes).

https://doi.org/10.1016/j.ijhydene.2023.07.001

Nickel foam
X-ray computed tomography
Compression
Structural and transport characteristics

ligament thickness, the mean pore size was found to decrease significantly with compression. The mean pore size is around 175 μm for uncompressed nickel foam and it decreased to around 110 μm for a 20% compression ratio and to around 70 μm for a 40% compression ratio. Further, unlike the effective diffusivity, the gas permeability was shown to be highly anisotropic with compression; this fact is of particular importance for PEFC modelling where the properties of GDLs are often assumed isotropic. All the computationally estimated properties have been presented, validated and discussed.

Introduction

The polymer electrolyte fuel cell (PEFC) is an electrochemical device that directly converts chemical energy into electrical energy [1–6]. The PEFC is a highly promising technology that could be utilised in the automotive industry due to its relatively high efficiency, quiet operation, fast refuelling and zero-emission at the point of use [7–12]. Consequently, in the past few years, PEFC-powered vehicles have attracted a significant deal of attention from the main automobile manufacturers [13–18]. Despite the early deployment stage of the PEFC technology, many technical barriers concerning the performance, reliability, durability and low cost need to be addressed [19–21].

A wet-proof, porous layer between the flow-field plate and catalyst layer is termed as the gas diffusion layer (GDL). The GDL plays a prominent role inside the PEFC in terms of being the exchange medium of mass, charge and heat between the catalyst layer and the flow channels grooved in the flow-field plate. The GDL should ideally: (i) provide sufficient air/oxygen gases to the active areas in the catalyst layers, (ii) ease the removal of the excess water, (iii) facilitate charge and heat transfer between the catalyst layer and flow-field plate and (iv) mechanically support the membrane [22–29]. The most commonly-used GDLs are prevalently of carbon paper or carbon cloth forms [30–33]. However, these traditional GDLs, particularly those used at the cathode side, are in general vulnerable to various types of degradation including: mechanical degradation (due to the clamping pressure), thermal degradation (due to the freeze/thaw cycles), carbon dissolution and erosion [34–38]. These degradations negatively affect the PEFC performance and the durability. Mechanical degradation is the most commonly type of degradation the GDL is subject to as its carbon fibres experience breakage, cracks and permanent deformation as a result of the assembly compression, thus leading to potential deterioration of the structural integrity of the GDL and reduced transport properties [39–43]. Hence, many researchers have been seeking alternative materials for the GDLs.

Metal foams have attracted a good deal of attention as promising materials used in various components in a multitude of energy engineering applications [44–46]. Recent studies have reported that nickel foam is a promising material for cathode flow field plates (FFP) and/or GDLs due to its superior properties such as: high porosity, excellent electrical and thermal conductivity, high cost-effectiveness, low weight-to-volume ratio and robust architecture. Hence, there have been only a few demonstrations in which the performance of the fuel cell equipped with nickel foam FFP has been compared to that of the conventional graphite FFP [47–55]. For instance, Tseng et al. [48] experimentally reported that the PEFC running with the nickel foam FFPs outperformed that running with the conventional FFPs and this is due to their superior mass transport properties of the former FFPs. Similarly, Liu et al. [53] experimentally showed that the fuel cell with a compressed nickel foam-based cathode FFP has a higher peak power density than that with a conventional graphite FFP, thus proposing nickel foam as a replacement material to graphite for FFPs. Furthermore, Tabe et al. [54] experimentally investigated the nickel foam-based FFP and their results indicated that nickel foam-based cathode FFP has, compared to the conventional FFPs, superior drainage ability and the fuel cell operating with it featured more stable operation at the higher current densities.

The performance of a PEFC is directly related to the structural and effective transport properties of the GDL materials. Thus, it has become indispensable to accurately determine these GDL properties and understand how they impact the operation behaviour of the PEFC under various operational conditions [56–59]. Moreover, the anisotropic nature of the GDLs must be assessed while the structural and transport properties are evaluated [40,60,61]. The structural and transport properties of the GDL might considerably differ between the through-plane and in-plane directions owing to the interior architecture of the material. To this end, numerous ex-situ methods are used to determine the structural properties of GDLs. For example, mercury intrusion porosimetry (MIP) is widely used to estimate the porosity and the pore size distribution of the GDLs [1,60,62]. Furthermore, the scanning electron microscope (SEM) is used to image the surface of the GDL to measure, for example, the fibre thickness [22]. The Brunauer-Emmett-Teller (BET) absorption technique is used to determine the specific surface area of the GDL [63,64]. Most of the above characterisation techniques are either destructive (e.g. focused ion beam) or do not provide insights into the interior structure of the GDLs. To illustrate, SEM typically provides high-resolution images; however, these images are only two-dimensional and superficial [40].

X-ray computed tomography (CT) is a highly versatile technique to provide detailed insight into the nano- or micro-scale morphological and transport characteristics of the PEFC components, including GDLs. The main advantages of X-ray CT are that it is: (i) non-destructive, (ii) relatively fast and

accurate, (iii) cost-effective, (iv) available for a wide variety of sample sizes and (v) allowing for investigation under the realistic operation conditions [65–67]. The commercial carbon-based GDLs have been widely investigated using the X-ray CT method to resolve the interior structure of the GDL [68–74]. This method has also been employed to understand the GDL structural properties under realistic fuel cell compression. For example, Zenyuk et al. [75] comprehensively investigated the morphological structures of various types of carbon-based GDLs (TGP, SGL, MRC and Freudenberg) by using X-ray CT tomography under compression. They evaluated the porosity, tortuosity, and pore size distribution under varying compression ratios; the researchers can then use these morphological into their numerical PEFC models. Similarly, Je et al. [76] investigated a Toray GDL using a compression apparatus hosted in an X-ray CT system. The porosity of the uncompressed GDL was found to decrease 0.79 by about 30% to be 0.56 with about 52% compression ratio. In addition, X-ray CT has been used to investigate the impact of compression on the nickel foam-based flow field fields used in PEFCs. For instance, Fly et al. [77] examined nickel foam as a flow field plate under different compression ratios using X-ray CT and finite element analysis. They showed that the fuel cell peak power density increased by 42% when increasing the compression from 20% to 70%. This improvement is because the penetration of nickel foam ligaments into the GDL increases with compression, thus allowing for more convective flow to reach the catalyst layer and better electrical contact between the nickel foam FFP and each of the GDL and the stainless-steel plate. Likewise, Wu et al. [78] investigated the nickel foam-based flow field plates under compression using X-ray CT. Their findings showed that the mean pore size decreased considerably with increasing compression ratios (6%, 37%, and 69%), while the porosity decreased insignificantly. Moreover, it was shown that the increased compression caused a higher pressure drop, higher airflow through the nickel foam and subsequently better removal of excess liquid water. In addition, the peak power density was found to be maximum with 37% compression ratio (853 mW/cm^2) and minimum with 6% compression (568 mW/cm^2).

To the best of our knowledge, there have been no studies investigating the impact of compression (that is normally encountered in operating PEFCs) on the structural and transport properties of nickel foam based using a non-distractive technique of X-ray CT. The above mentioned conventional characterisation techniques (e.g. SEM and MIP) cannot be used to determine the properties of the GDL under compression [75]. Ercelik et al. [79] investigated the potential use of nickel foam as a GDL for PEFCs using X-ray CT. They developed computationally economic X-ray CT image-based two-dimensional models to determinate the key structural and transport properties of the nickel foam-based GDL. As a valuable and important extension to this investigation, the objective of the present study is to evaluate the structural (the porosity, tortuosity, pore size distribution, ligament thickness distribution, and the specific surface area) and transport (gas permeability and effective diffusivity) of nickel foam based GDLs under compression ratios normally encountered in operating PEFCs. Furthermore, the anisotropic nature of the nickel foam-based GDL under compression is evaluated. To achieve this, a specially designed compression apparatus was manufactured through 3D printing and used in an X-ray CT chamber to image the compressed nickel foam. The X-ray CT-based images are then used to create computationally economic 2D models. It should be noted that the thermal and electrical conductivities of nickel foams are also important characteristics. However, as they are orders of magnitudes higher than those of carbon fibre based GDLs, they are not expected to form rate limiting factors for the fuel cell performance and as such they were not investigated in this study. Nonetheless, this may be a possible research topic for a future work. The findings of the study are of great interest to the modellers and developers of PEFCs, as they represent realistic values for the structural and mass transport properties of the nickel foam-based GDLs under compression levels that are normally encountered in real-life fuel cells. Namely, they could be employed in the PEFC models to improve the accuracy of the predictions and provide reliability to the respective optimisation studies.

Methodology

Compression apparatus

A special compression apparatus was designed, manufactured, and used inside an X-ray CT chamber (Fig. 1) in order to investigate the structural and transport properties of the nickel foam based GDL under compressions that the GDL is subject to inside the PEFC. The apparatus parts were designed using SolidWorks® 2015 and manufactured using Ultimaker 2+ Extended® 3D printer (Ultimaker, Cambridge, MA, US). The material for 3D printing was polylactic acid (PLA) which possesses high X-ray radiolucent characteristic. Likewise, nylon M5 bolts, nuts and washers were employed owing to their X-ray transparency properties.

X-ray CT and image processing

SKYSCAN 1172 (Bruker US) X-ray microscopy system was employed during the X-ray CT imaging process. This system consists of an X-ray source, a detector and a rotational stage where the compression apparatus is fixed. The emitted X-ray from the source traversed through the sample and the detector captured the X-rays weakened due to solid ligaments. Fig. 2 shows the main components of the X-ray CT system. A commercially available nickel foam sheet with 99.5% purity (Goodfellow Cambridge Ltd., the UK) was punched to create a 12.7 mm diameter sample. The sample was carefully located in the compression apparatus and the apparatus was then fixed on the rotational stage. The scanning processes were performed every time the stage was rotated by 0.7° until the full 180° rotation was reached. The exposure time was 0.885 s and 1025 projections were collected for each scanning. The source voltage was 80 kV, and the beam current was 124 μA. The image resolution was 7 μm per pixel. The compression of the apparatus was increased step by step after each scanning.

The 2D shadow images were obtained and processed using the NRecon Reconstruction software (SKYSCAN,

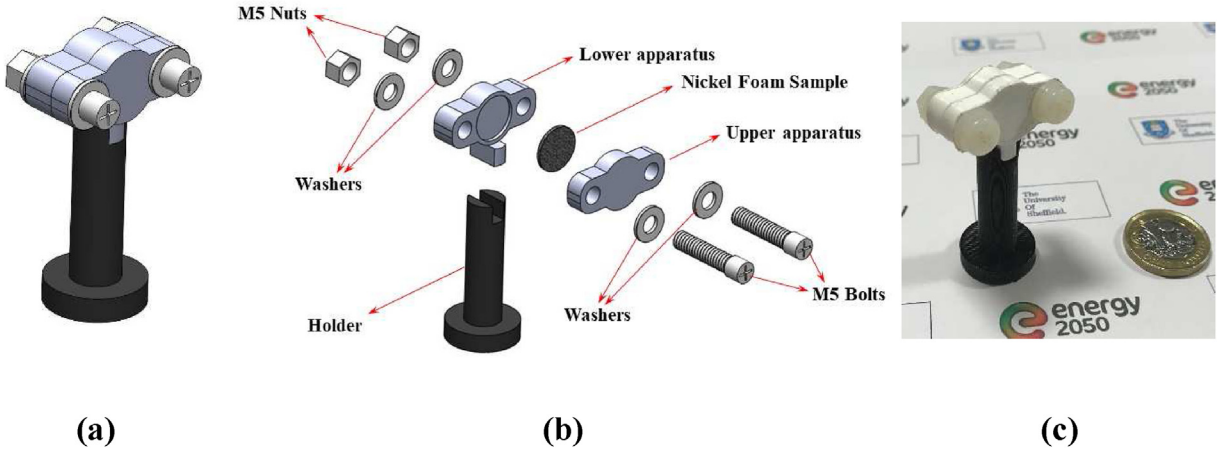

Fig. 1 – (a) The designed compression apparatus, (b) the exploded view and the main components of the apparatus and (c) the manufactured compression apparatus.

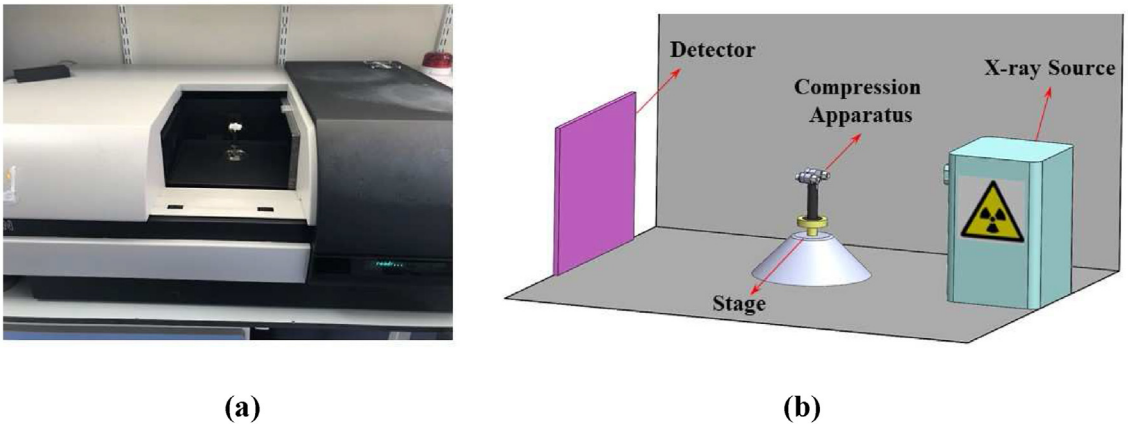

Fig. 2 – (a) SKYSCAN X-ray CT system and (b) its main components.

Belgium) to reconstruct the cross-sectional images from the X-ray CT projection images. The images were then processed using Bruker CTan Micro-CT where Otsu's thresholding method was employed to separate the solid and void phases. Finally, the processed images were imported to COMSOL Multiphysics® 5.5 using MATLAB® and LiveLink™ for MATLAB®.

Numerical modelling

The continuity and momentum conservation equations were solved within COMSOL Multiphysics® 5.5 for 20 equally spaced X-ray CT slices with a 350 μm distance for each compression level of nickel foam. It is noteworthy that we investigated the effect of the number of slices (from a range that starts with 5 slices and ends with 30 slides) on the structural and transport properties of the nickel foam in the supplementary material; see Figures S.1 to S.8. It was shown that the values of the structural and transport properties of the nickel foam starts to saturate with 10 equally spaced X-ray CT slices. Therefore, the selected number of equally spaced X-ray CT slices (i.e. 20) should be highly representative of the nickel foam material. The length of each slice was 6.65 mm and the height changed depending on the compression applied. Namely, the heights were 1.05, 0.84 and 0.63 mm for 0, 20 and 40% compressions respectively; the 3D X-ray CT-based representations of the nickel foam under the abovementioned compressions are shown in Fig. 3. Notably, the heights of these samples (and compression ratios) are determined by systematically and gradually tightening the M5 bolts in a step-by-step manner, taking into account the value of the screw pitch.

The flow regime in the computational domains was assumed to be steady-state, incompressible (Mach numbers « 0.3) and laminar Reynolds numbers « 2300. Thereby, the continuity and momentum conservation equations can be given as follows:

$$\nabla\cdot(\rho\boldsymbol{u}) = 0 \tag{1}$$

where ∇ is the operator $(i\frac{\partial}{\partial x} + j\frac{\partial}{\partial y})$, ρ is the fluid density (kg/m^3) and $\boldsymbol{u}$ is the velocity vector.

$$\rho(\boldsymbol{u}\cdot\nabla)\boldsymbol{u} = \nabla\cdot\left[-pI + \mu\left(\nabla\boldsymbol{u} + (\nabla\boldsymbol{u})^T\right) - \frac{2}{3}\mu(\nabla\cdot\boldsymbol{u})I\right] \tag{2}$$

where p is the pressure, I is the identity matrix and μ is the

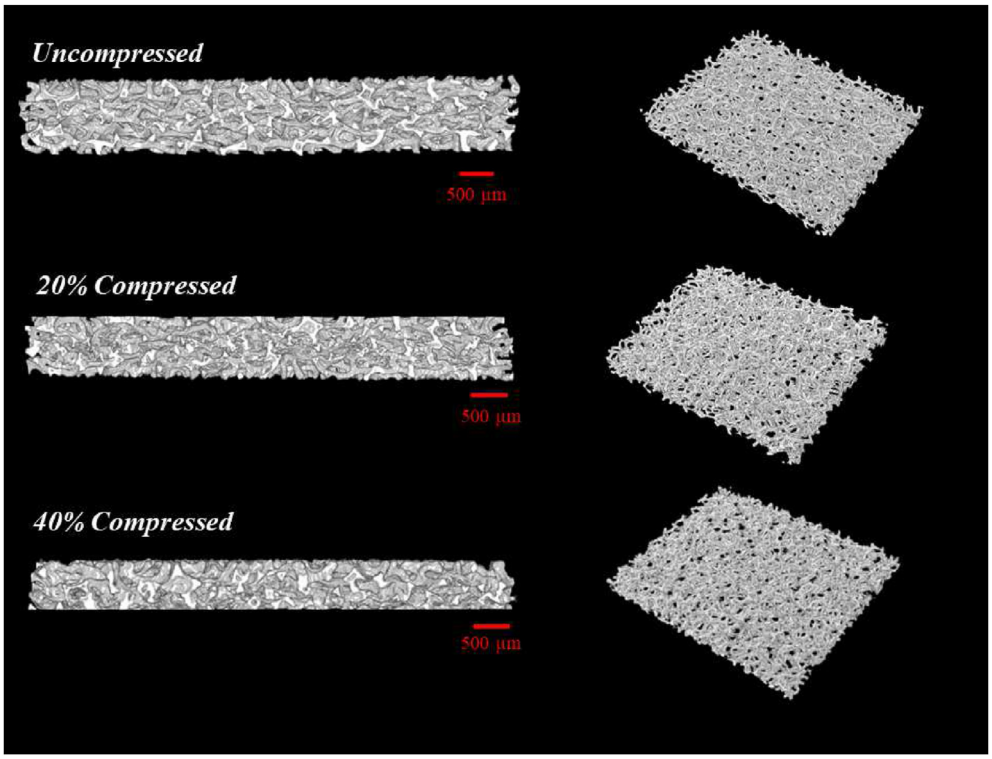

Fig. 3 – The three-dimensional X-ray CT representations of the nickel foam at 0, 20 and 40% compressions.

dynamic viscosity (Pa·s). The conservation of chemical species, which is oxygen in our case, is expressed as follows:

$$\nabla\cdot(-D_{O2}\nabla C_{O2}) = R \quad (3)$$

where D_{O2} is the oxygen diffusion coefficient (m^2/s), C_{O2} is the oxygen concentration (mol/m^3), and R is the source term which is zero in our case (there is no reaction taking place within the GDL).

The 20 CT slices were meshed within COMSOL Multiphysics® 5.5 at each level of compression. All the computational domains were checked for mesh-independent solutions. Fig. 4 exhibits how the through- and in-plane gas permeabilities (and the corresponding computation time) change with the number of element numbers for an arbitrarily selected 20% compressed slice (the 200th Slice). The computed permeability values were shown to be almost insensitive to the number of elements beyond around 550,000 elements and the corresponding computation times were found to be relatively short: around 100 s. Overall, the mesh-independent solutions for all the 20 computational domains were found to be between 400,000 and 700,000; Fig. 5 shows a typical meshed computational domain along with the boundary conditions used to solve the models.

The gas flowing through the nickel foam was assumed to be air which is the normally used oxidant at the cathode of the PEFCs. As for the gas permeability investigation, the inlet air velocity and outlet pressure were arbitrarily set as 0.1 m/s and 0 Pa, respectively. Notably, under relatively low flow rates (Darcy's regime), the pressure gradient linearly changes with the inlet air velocity and as such the gas permeability, which is an intrinsic property of the material, evidently does not change with velocity as demonstrated in Figures S.9 and S.10 in the supplementary material. Moving to the effective diffusivity investigation, the inlet air (molar fraction-wise) consists of 21% oxygen and 79% nitrogen. Hence, the inlet concentration of oxygen (C_{in}) is 8.73 mol/m^3 at 20 °C and 1 atm whereas the outlet concentration was assumed to be 7.73 mol/m^3. It should be noted that there is no impact of the concentration difference on the estimated effective oxygen diffusivity since the molar flux of oxygen proportionally changes with the concentration difference; see Table S.1, Table S.2, and Figure S.11. The bulk oxygen diffusivity coefficient is 0.219 cm^2/s at 20 °C and 1 atm. Equations (2) and (3) are solved independently for each direction (i.e. through- and in-plane directions) to estimate the gas permeability and effective oxygen diffusivity for each direction. It should be noted that, to estimate the effective diffusivity of the porous media, Equation (3) disregards the convective term. This is because solving the equation considering only the diffusive term is sufficient to obtain the effective diffusivity of the porous media. Given that the effective diffusivity is an intrinsic property of the material, adding the convective term to the equation would unnecessarily complicate the solution without any gain in accuracy.

The boundary conditions used for the models are shown in Fig. 5. Namely, the top edge was defined as an inlet while the bottom was set as an outlet for the through-plane direction analyses. In addition, the right and the left edges were prescribed as symmetry boundary conditions. On the other hand, the left and the right edges were defined as an inlet and an outlet for the in-plane direction analyses, respectively, whereas the top and the bottom edges were set as walls. Furthermore, the borders surrounding the ligaments were defined as no-slip boundary conditions. It should be noted

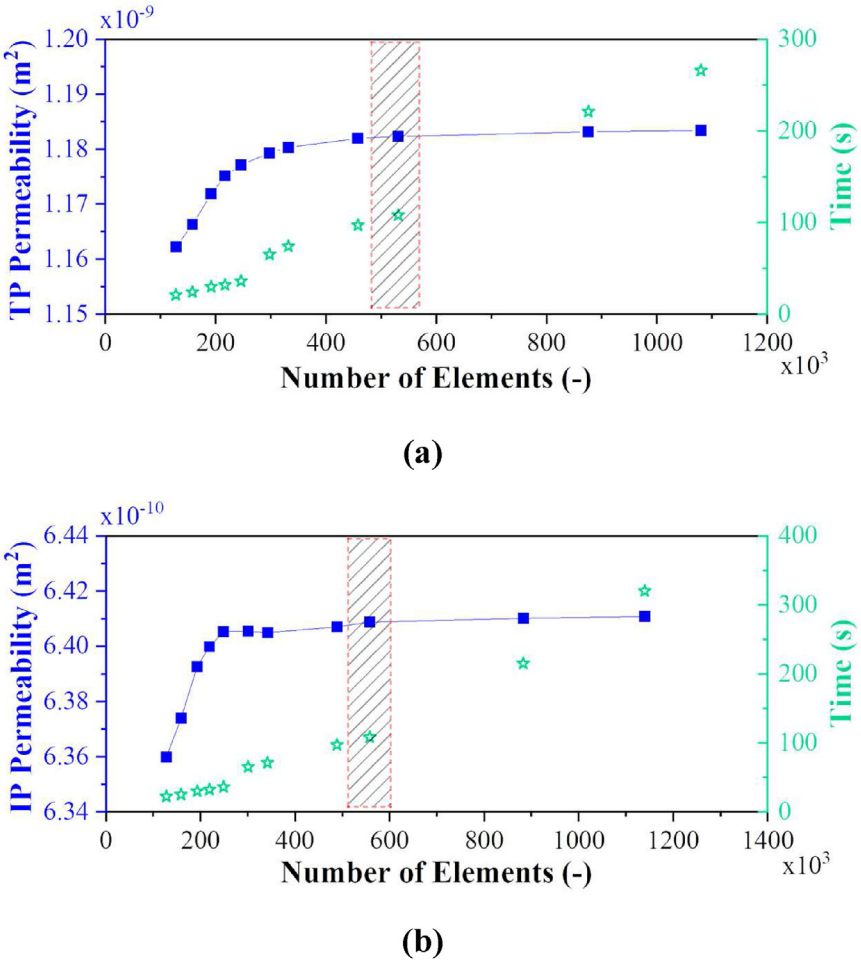

Fig. 4 – (a) The through-plane and (a) in-plane permeabilities (and the corresponding computation time) as they change with number of elements for a 20% compressed CT slice (the 200th slice). The shaded areas highlights the number of elements with which the mesh-independent solutions are realised.

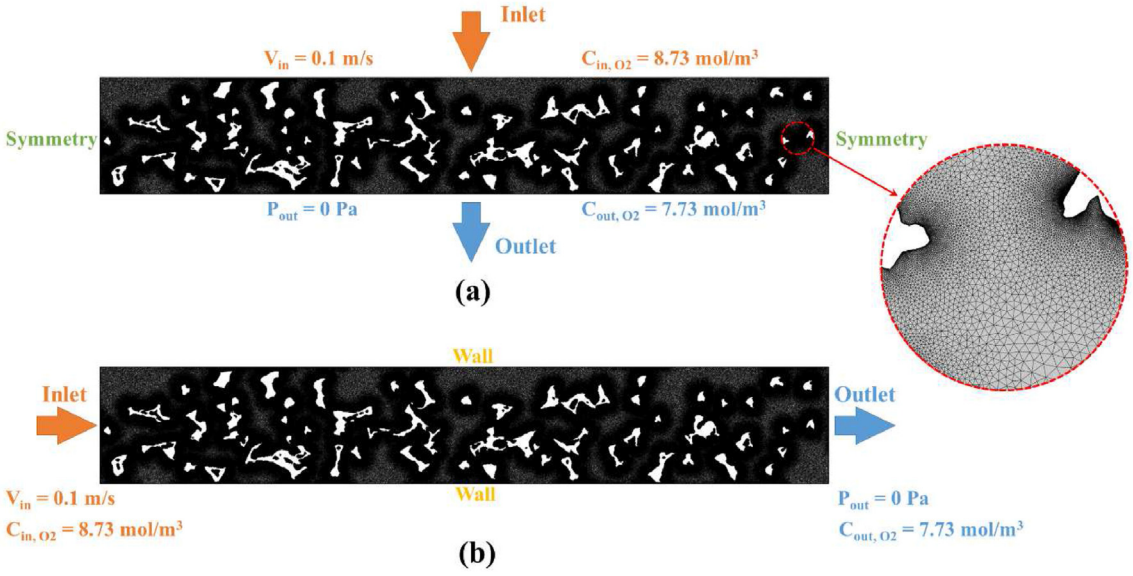

Fig. 5 – The boundary conditions and the meshed computational domain for (a) through-plane and (b) in-plane directions. The white areas are the solid phase (i.e. the ligaments of the nickel foam).

that the numerical simulations were conducted assuming that the inlet temperature is 20 °C. The models were numerically solved using a small-scale workstation (Inter® Xenon® CPU E3-1246 v3@ 3.50 GHz, 16 GB installed RAM), and the computational time for each modelled CT slice was found to be between 100 and 200 s.

Structural properties

Porosity

The porosity (ε) is a structural property of the medium that represents the ratio between the volume of the void and the total volume of that material. The transport properties (e.g. gas permeability and effective diffusivity) strongly depend on the porosity and typically decline with decreasing porosity. On the other hand, the electrical and thermal conductivities are inversely proportional to the GDL porosity. Many experimental methods, such as mercury intrusion porosimetry (MIP) or other standard porosimetry techniques, are normally used to measure the GDL porosity. However, these methods are not feasible to investigate the same sample under different compression levels and this is due to the existence of mercury in the pores of the sample from previous lower-in-compression tests. Therefore, these techniques are mainly used to measure the porosity of uncompressed GDL materials [75]. On the other hand, the X-ray CT provides insight into the interior structure and inhomogeneity of the GDL with/without realistic compressions. The maximum reported porosity of an uncompressed carbon fibre-based GDL is about 0.90 [1,80], whereas the maximum reported porosity of an uncompressed nickel foam porosity is 0.98 [81]. Evidently, increasing the compression on the GDL decreases its porosity. In this study, the porosity values for a nickel foam-based GDL under three compression ratios were determined for 20 equally spaced X-ray CT slices using the COMSOL Multiphysics® 5.5. This was achieved through measuring and summing the areas for each of the void and the solid phases and then dividing the total area of the void phase by the total area of the slice:

$$\varepsilon = \frac{Total\ area\ of\ void\ phases}{Total\ area\ of\ slice} \tag{4}$$

For comparison purposes, the porosity was also theoretically calculated using the following equation:

$$\varepsilon_{theo} = \frac{\varepsilon_0 - X_{comp}}{1 - X_{comp}} \tag{5}$$

where ε_{theo} is theoretical porosity, ε_0 is the uncompressed porosity, and X_{comp} is the compression ratio of the compressed nickel foam. It should be noted that, in Equation (5), it is assumed that only the void that decreases with compression [77].

Tortuosity

Tortuosity is a structural characteristic that denotes the ratio of the actual length of the flow path to the straight path between the two ends of that path [82]. In other words, tortuosity equals to unity if the flow path is straight, and tortuosity more than unity mean that the flow needs to travel longer distance than that of the fictitious straight path of the flow. Furthermore, the tortuosity provides information on how the pores are interconnected within the porous medium. The tortuosity values for through- and in-plane directions within a two-dimensional CT slice can be obtained using the following equations [83]:

$$\tau_{Through-plane} = \frac{u_{mag}}{u_y} \tag{6}$$

$$\tau_{In-plane} = \frac{u_{mag}}{u_x} \tag{7}$$

where u_{mag} is the velocity magnitude averaged over the computational domain, and u_y and u_x are the velocity components in the through- and in-plane directions, respectively.

Pore size distribution

The pore size distribution of the nickel foam-based GDL considerably affects the transport properties of reactant gases and liquid water. Large pores within the foam ease the transverse of fluids from one cell to another. The pore size distributions for all the compression cases for all the 20 CT slices were determined using an open-source ImageJ/Fiji software [84]. Unlike SEM images, which only show the superficial morphology, three-dimensional or multiple two-dimensional CT images allow for the access to the interior structure of the compressed/uncompressed porous material.

Ligament thickness distribution

Ligaments (or struts) are the solid metal rods that constitute the cellular web-like structure of the nickel foam. The structures and thicknesses of the ligaments could significantly affect the electrical and thermal conductivity and the mechanical integrity of the foam. As with the pore size distribution, the ligament thickness distribution for the all the 20 CT slices under all the investigated three compression ratios were determined using the ImageJ/Fiji software [84].

Specific surface area

The specific surface area (SSA) can be defined as the surface area per the volume unit. As with all the structural properties, the specific surface area of the nickel foam impacts the mass, heat and charge transport within it [85,86]. The nickel foam typically possesses a high specific surface area due to its web-like cellular architecture. However, this property expectedly increases with increasing compression [87]. The total length of the borders of the solid phase and its areas were measured for all the 20 CT slices under the three investigated compression ratios using COMSOL Multiphysics®.

Mass transport properties

Gas permeability

The gas permeability represents how permeable the porous media is. It is an important GDL property particularly at the cathode side. High gas permeability leads to lower pressure gradients within the GDL and subsequently lower water saturation, thus mitigating the water flooding phenomena [88–90]. Furthermore, high gas permeability enhances the convective flow from the flow channels to the catalyst layer, the availability of reactant gases and, therefore, the PEFC performance [1,91–93]. The GDLs within the fuel cell are

under compression and therefore the transport properties should be quantified under that compression to obtain more accurate values for these transport properties. For this purpose, the through- and in-plane gas permeability for nickel foam under a realistic set of compression ratios were obtained through solving Equations (1) and (2) that were applied to the two-dimensional CT-based computational domains. For low velocities, the viscous resistance is dominant and the inertial resistance is negligible. Therefore, the linear Darcy's Law (rather than the quadratic Forchheimer equation) was used to estimate the permeability values of the porous medium:

$$\frac{\Delta P}{L} = \frac{\mu}{K} u \tag{8}$$

where ΔP denotes the pressure difference between the inlet and outlet boundaries, L is the length of the GDL material across the flow length, μ is the dynamic viscosity of the flowing fluid (air), K is the gas permeability of the porous medium and u is the inlet gas velocity. L represents the length of the nickel foam GDL (i.e. 6.65 mm) for in-plane gas permeability simulations and represents its thickness (i.e. 1.05, 0.84 and 0.63 mm for 0, 20 and 40% compression ratios) for the through-plane gas permeability simulations. The dynamic viscosity of air (μ) at 20 °C and 1 atm is 1.751×10^{-5} Pa s [94]. The inlet velocity of the computational domain (u) has been set as 0.1 m/s for each compression ratio. It is noteworthy that the sensitivity of gas permeability to relatively low inlet gas velocities are almost negligible, as shown in Figure S.9 in the supplementary material; this figure shows that the pressure gradient scales linearly with the inlet velocity under different compression ratios. Similarly, Figure S.10 demonstrates that the gas permeability negligibly changes with inlet velocity under different compression ratios.

Effective diffusivity

Diffusion within the GDL plays a significant role in transporting reactant gases between the flow channel and the catalyst layer; this role is more profound for the conventional carbon fibre-based based GDLs and this is due to their low gas permeability values [23–25,31,92,95,96]. The effective diffusivity represents how chemical species diffuse into each other within a porous medium. The effective diffusivity of oxygen into nitrogen in a porous GDL can be estimated by Fick's Law:

$$J = D^{eff}_{O2,N2} \frac{\Delta C}{L} \tag{9}$$

where J is the oxygen molar flux (mol/(m^2·s)), ΔC is the oxygen concentration difference between the inlet and outlet across the thickness (for through-plane diffusivity simulations) or length (for in-plane diffusivity simulations) of the GDL. As with the gas permeability simulations, L is the length of the nickel foam GDL (6.65 mm) for the in-plane diffusivity simulations and is the GDL thickens (i.e. 1.05, 0.84 and 0.63 mm for 0, 20 and 40% compression ratios) for the through-plane diffusivity simulations. The oxygen concentration difference (ΔC) is assumed to be 1 mol/m^3 for each compression scenario. It is noteworthy that (as shown in Table S.1, Table S.2, and Figure S.11 in the supplementary material) the oxygen concentration difference does not impact the effective diffusivity since the oxygen molar flux changes proportionally with the concentration difference of oxygen.

Results and discussion

The velocity profiles of the flowing air through the uncompressed, 20% compressed, and 40% compressed nickel foam-based GDL are shown in Figures (6) and (7) for the through- and in-plane directions, respectively. In general, the position and the thickness of the ligaments considerably affect the magnitude of the air velocity and the direction of the flow, resulting in relatively high non-uniform velocity profiles. It is evident from Figures (6) and (7) that the velocity magnitudes, in either the through- or in-plane directions, become higher as the compression ratio increases. This is understandable due to the fact that the voids between the ligaments are closed up due to the compression resulting in smaller flow openings and subsequently higher local velocities for a given boundary flow rate.

Porosity

The porosity values for all the 20 equally spaced X-ray CT slices are shown in Fig. 8(a) for three different compression ratios. The mean porosity value for the uncompressed sample is 0.894 ± 0.008 and it varies between 0.861 and 0.921. This value is highly consistent with the experimental results reported in the literature for nickel foam material. For instance, Oun and Kennedy [87] experimentally estimated the porosity of uncompressed nickel foams and found it to be 0.88. The range of porosity for uncompressed nickel foams was investigated utilising 3D X-ray CT imaging by Vicente et al. [97] and was reported to be between 0.87 and 0.92. Clearly, as the compression increases, the porosity of the metal foam decreases. The mean porosity range for 20% compressed nickel foam is 0.866 ± 0.007 and it varies between 0.84 and 0.90. The porosity continues to slightly decrease with 40% compression and becomes 0.842 ± 0.011 and it varies between 0.799 and 0.883. As with the uncompressed nickel foam case, the results are highly consistent with the porosity values reported in the literature. For example, Fly et al. [77] investigated the nickel foam flow field plates using 3D X-ray CT imaging and reported the porosity for uncompressed, 17% compressed and 35% compressed nickel foams as 0.892, 0.875, and 0.834, respectively.

Furthermore, the actual (obtained from the new X-ray CT-based method) and the theoretical (obtained from Equation (5)) porosity of the nickel foam sample are shown in Fig. 8 (b). It is clear that there is a very good agreement between the actual and the calculated values of the porosity for the uncompressed and 20% compressed nickel foam cases. However, the theoretical porosity is slightly less than the actual porosity at 40% compression. The reason behind this discrepancy is that Equation (5) assumes that the volume reduction of the void only takes place in the open spaces between the ligaments. However, there exists isolated voids between the ligaments that are normally created as a result of the corresponding manufacturing process. The reduction in volume of these isolated voids are not included in Equation (5), thus resulting

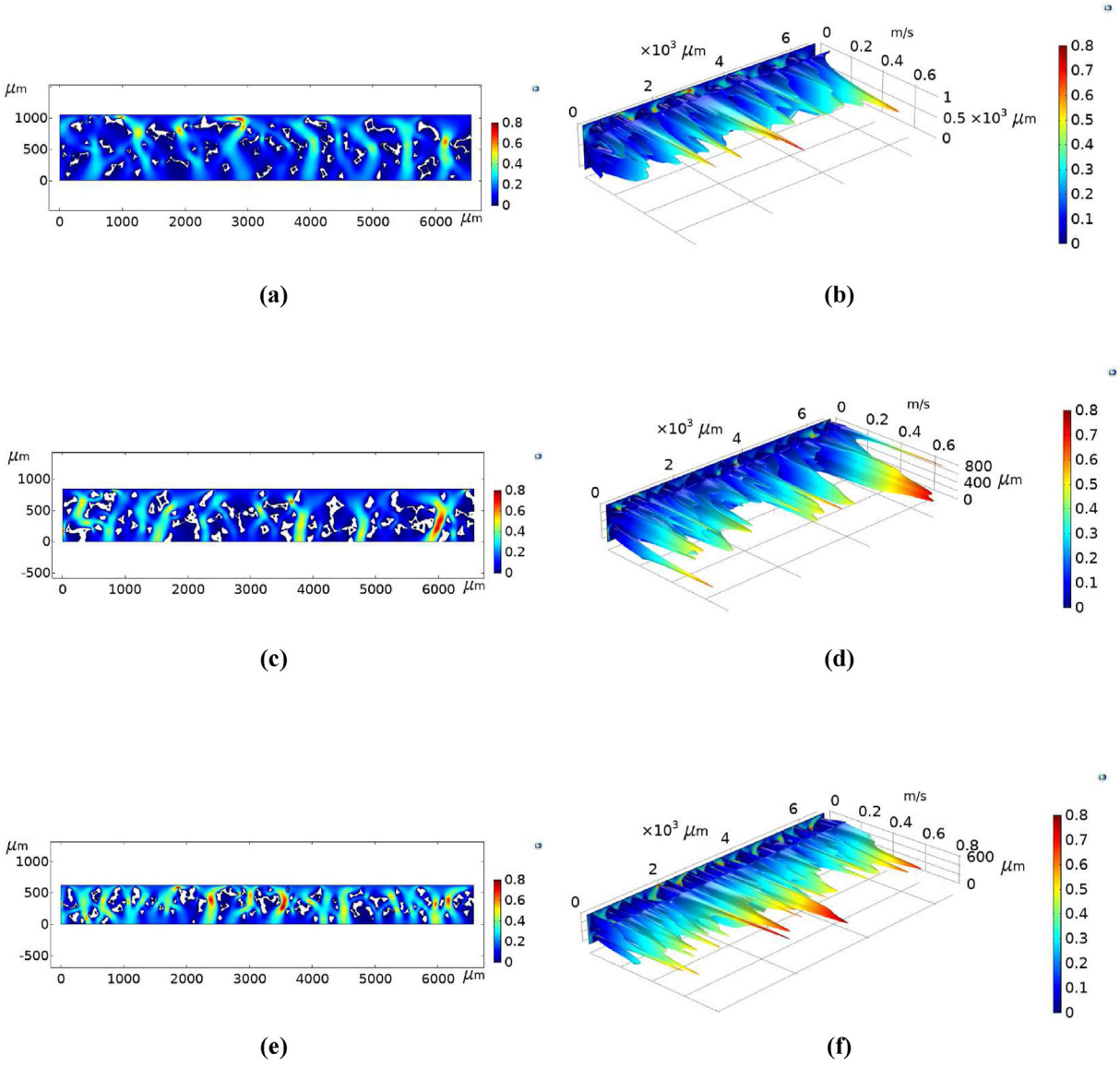

Fig. 6 – The through-plane velocity profiles for the 100th slice under uncompressed (a and b), 20% compressed (c and d), and 40% compressed (e and f) situations.

in the underestimation of the porosity of the nickel foam subject to the relatively high compression (i.e. 40%).

Tortuosity

The tortuosity in the through- and in-plane directions for all the 20 CT slices are shown in Fig. 9 for the three investigated compression ratios. The mean through-plane tortuosity for the uncompressed situation is 1.179 ± 0.011. This value is in very good agreement with those reported in the literature: Khayargoli et al. (i.e. 1.15) [98], Ercelik et al. (i.e. 1.175) [79] and Langlois and Coeuret (i.e 1.15 ± 0.10) [99]. The in-plane tortuosity of the uncompressed nickel foam is 1.138 ± 0.011 and therefore is slightly lower than that of the through-plane direction. As with the through-plane tortuosity, the computed in-plane tortuosity of the uncompressed nickel foam is in very good consistence with those reported in the literature, which were found to be between 1.09 and 1.13 [100]. It should be noted that the tortuosity values of the conventional carbon fibre based GDLs are considerably higher than those of the nickel foam. For example, the minimum tortuosity values for the SGL and Toray GDLs were reported to be 1.33 and 2.50, respectively [22]. With 20% compression ratio, the mean through- and in-plane tortuosity values, compared to those of the uncompressed foam, increase to 1.20 ± 0.022 and 1.168 ± 0.022, respectively. It is evident that the voids between the ligaments are closed up with increasing compression, thus leading to more tortuous paths throughout the foam. As the compression increases to 40%, the mean values of the through- and in-plane tortuosity become closer to each other: they are 1.184 ± 0.017 and 1.189 ± 0.014, respectively. One may notice that the in-plane tortuosity increases as the compression increases from 0 to 40%; however, the through-plane tortuosity was found to increase as the compression

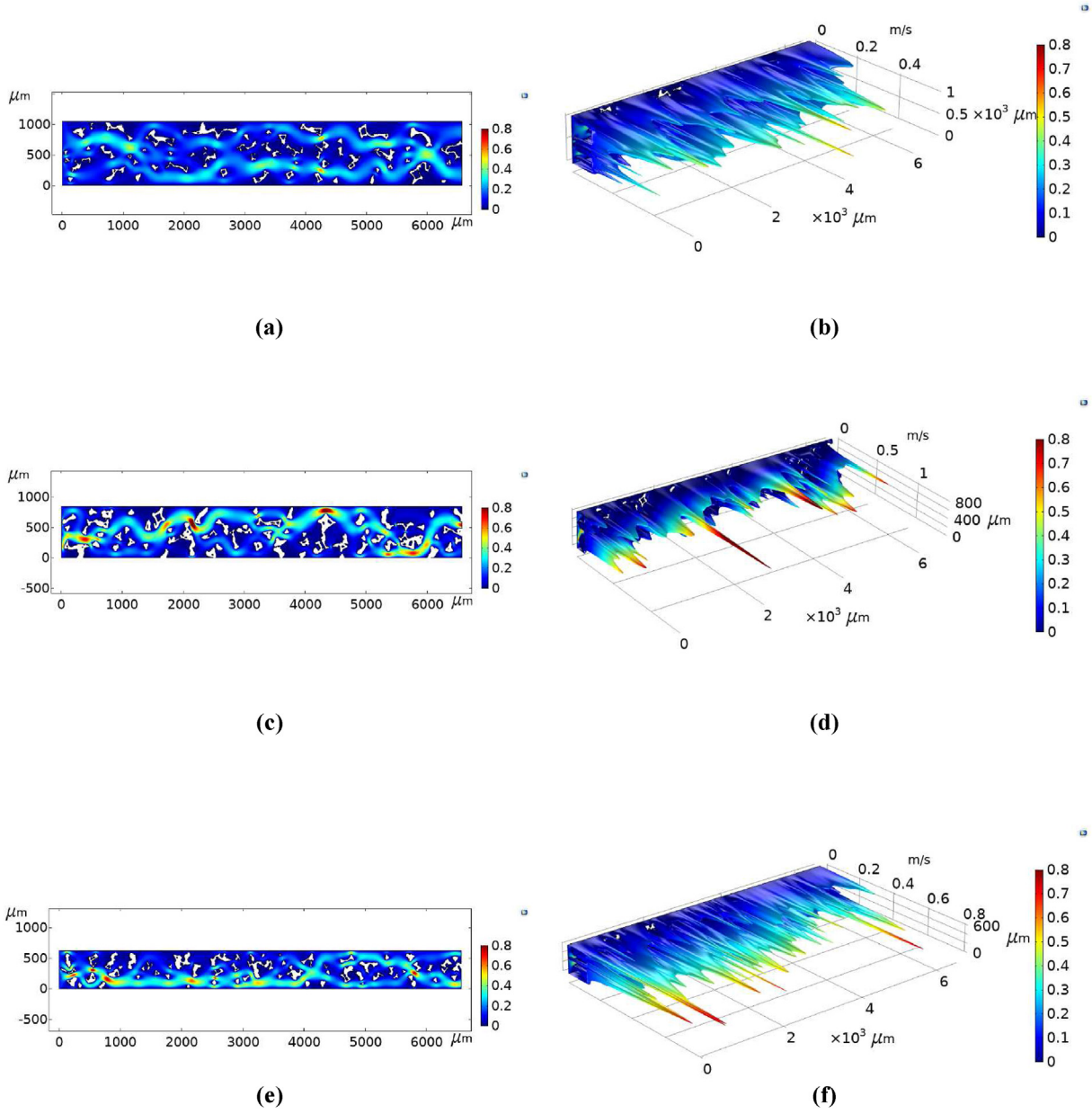

Fig. 7 – The in-plane velocity profiles for the 100th slice under uncompressed (a and b), 20% compressed (c and d), and 40% compressed (e and f) situations.

increases from 0 to 20% and then decrease as the compression increases from 20 to 40%. This could be attributed to the observation that the structure of the nickel foam is more or less "nest-like" and therefore the "entanglement" of the ligaments, which is mainly in the in-plane directions, increases with increasing compression. On the other hand, the through-plane pathways appear to straighten after a certain threshold compression.

Pore size distribution

The pore size values for all the 20 CT nickel foam slices are shown in Fig. 10 for the uncompressed, 20% compressed, and 40% compressed cases. The pore size histograms of all the cases (60 cases representing 20 CT slices and 3 compression ratios) are shown in Figures S.12 to S.14 in the supplementary material. The mean pore size value of the uncompressed nickel foam is 175 ± 5 μm and the range of pore sizes is between 151 and 217 μm. The mean pore size of the uncompressed nickel foam is in very good agreement with those reported in the literature; for example Miwa and Ravankar [101] reported the mean pore size of some nickel foam samples as a range of from 172 μm to 182 μm while Milazzo et al. [102] measured it as 230 μm. The mean pore size and the lower and the upper limits of its range expectedly decrease with increasing compression due to reduction in the volume of voids of the nickel foam. Namely, the mean pore size, with 20% compression, decrease to 110 ± 4 μm for and the limits of the range decrease to 92 and 119 μm. Likewise, the mean pore

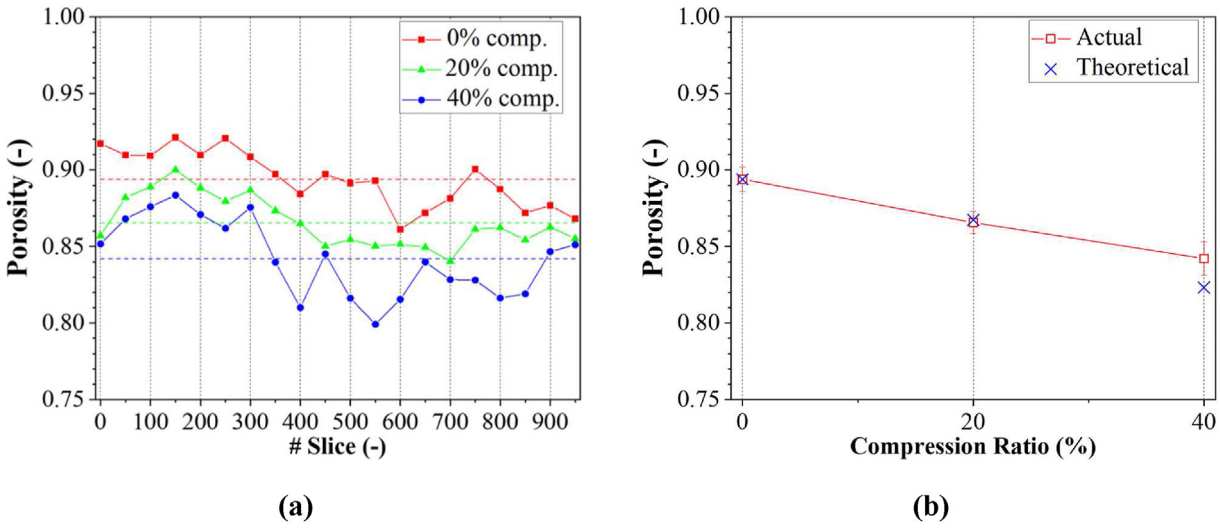

Fig. 8 – (a) Porosity values for the uncompressed, 20% compressed, and 40% compressed CT nickel foam slices and (b) the actual and theoretical porosity of nickel foam. Note that the error bars represent 95% confidence intervals.

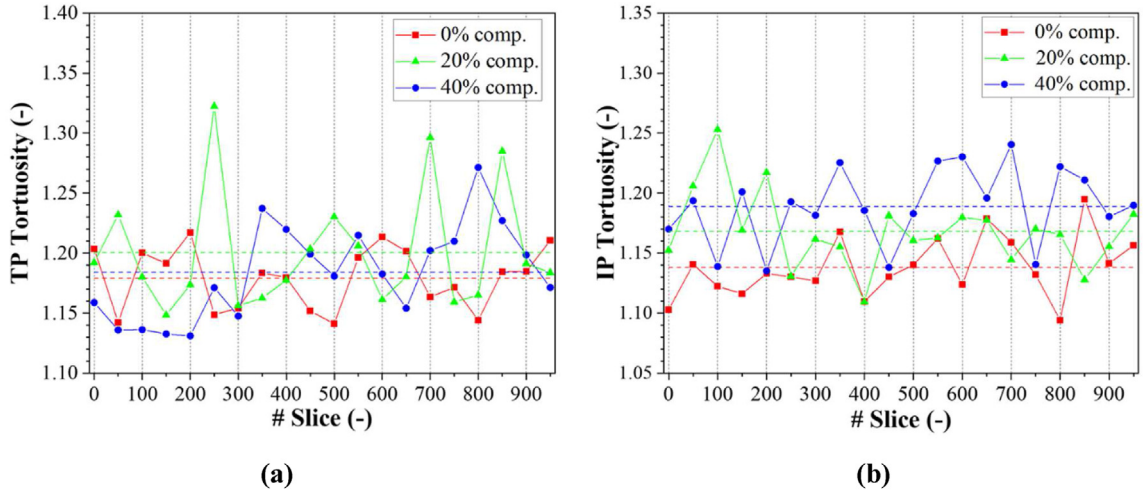

Fig. 9 – (a) Through-plane and (b) in-plane tortuosity values for the uncompressed, 20% compressed, and 40% compressed CT nickel foam slices.

size decrease to 71 ± 2 μm and the limits of its range decrease to 55 and 81 μm with 40% compression.

Ligament thickness distribution

The ligament thickness values for all the 20 CT nickel foam slices are presented in Fig. 11 for the uncompressed, 20% compressed, and 40% compressed cases. The histograms of the ligament thickness distribution are shown in the supplementary material; see Figures S.15 to S.17. The mean ligament thickness is 100 ± 1 μm for the uncompressed nickel foam, which is in very good agreement with those reported in the literature. For instance, Miwa and Revankar [101] found that the mean ligament thickness of nickel foam is between 99 and 107 μm. Interestingly, the ligament thicknesses were found to significantly decrease with increasing compression; the mean ligament thickness decreases to 96 ± 1 with 20% compression and to 90 ± 1 μm with 40% compression. This is primarily due to the fact that the ligaments are not entirely solid and they enclose some void that shrinks as the compression increases.

Specific surface area

Fig. 12 displays the specific surface area (SSA) for all the 20 CT nickel foam slices for the uncompressed, 20% compressed, and 40% compressed cases. The mean specific surface area of the uncompressed nickel foam is 55700 ± 2700 m^{-1}. The specific surface area increases with increasing compression (due to the evident volumetric decrease); it increases to 57100 ± 2800 m^{-1} with 20% compression ratio and to 61000 ± 2900 m^{-1} with 40% compression ratio. These results are in accordance with the findings reported in the literature that shows that the specific surface are of nickel foams increase with increasing compression [103–105]. High specific surface area is expected to increase mass transport resistance; this will be touched on in the following section. On the other

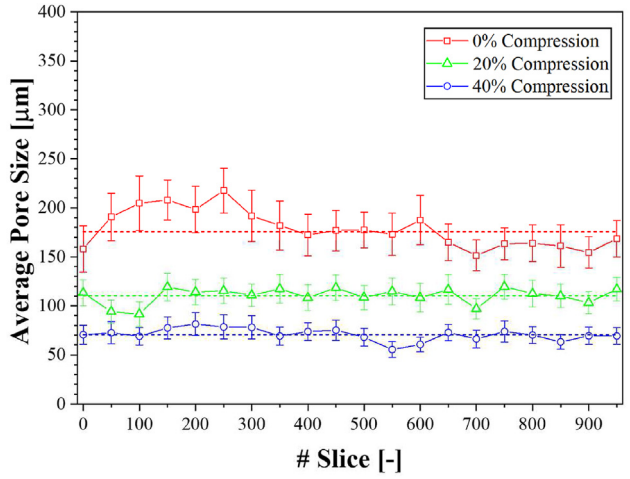

Fig. 10 – Mean pore size for the uncompressed, 20% compressed, and 40% compressed CT nickel foam slices. Note that the error bars represent 95% confidence intervals.

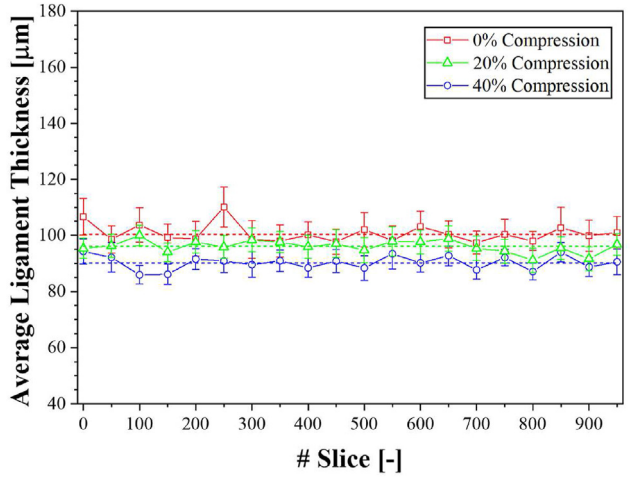

Fig. 11 – Mean ligament thickness for the uncompressed, 20% compressed, and 40% compressed CT nickel foam slices. Note that the error bars represent 95% confidence intervals.

hand, high specific area areas are favourable for the electrical and the thermal conductivity as well as the electrical contact with either the catalyst layer or the flow-field plate [106,107].

Gas permeability

The gas permeability values for all the 20 CT nickel foam slices were computationally estimated under the three compression ratios: 0, 20 and 40%; see Fig. 13. The average through- and in-plane permeability values were respectively computed to be 1.63×10^{-9} and 1.64×10^{-9} m^2 for the uncompressed nickel foam. The mean through-plane and in-plane permeability values are very close to each other, and this signifies the high isotropy of the uncompressed nickel foam; the anisotropy ratio (which is the ratio between the through- and the in-plane transport properties) is almost one. Fig. 13 shows that the through-plane permeability of the CT nickel slices vary between 1.02×10^{-9} and 2.17×10^{-9} m^2. Likewise, the corresponding in-plane permeability varies between 1.12×10^{-9} and 2.31×10^{-9} m^2. These permeability values are in very good agreement with those reported in the literature. For instance, Khayargoli et al. [98] and Medraj et al. [108] experimentally estimated the through-plane permeability to be around 1.30×10^{-9} m^2. Gerbaux et al. [109] experimentally estimated the in-plane permeability of nickel foam as 1.94×10^{-9} m^2. Likewise, Topin et al. [110], Hugo et al. [111], and Bonnet et al. [45] measured the in-plane permeability as 1.38×10^{-9}, 1.38×10^{-9} and 1.85×10^{-9} m^2, respectively. It is noteworthy that the gas permeability of the uncompressed nickel foam-based GDL is at least two orders of magnitude higher than the conventional carbon fibre based GDLs [22]. The permeability is evidently decrease with compression; see Fig. 13. The mean through- and in-plane permeability of the 20% compressed nickel foam are respectively 9.96×10^{-10} and 6.89×10^{-10} m^2, and the lower and the upper limits are 1.39×10^{-10} and 6.48×10^{-10} m^2 for the through-plane permeability and 5.09×10^{-10} m^2 and 1.08×10^{-9} m^2 for the in-plane permeability. Clearly, as shown in the "porosity" and "pore size distribution" subsections of the "results and discussion" section, compression decreases the pores between the ligaments and, subsequently, the porosity of the foam. It is well-known that gas permeability decreases with decreasing porosity as evident from Carman-Kozney equation [112]. With 40% compression ratio, the mean through- and in-plane permeability values further reduce to 5.57×10^{-10} and 3.51×10^{-10} m^2 respectively, and the lower and upper limits decrease to 3.07×10^{-10} and 8.69×10^{-10} m^2 for the through-plane permeability and to 1.21×10^{-10} and 6.68×10^{-10} m^2 for the in-plane permeability. Notably, the permeability in the in-plane direction is more sensitive to compression than that in the through-plane direction as compression increases to 20; this is more evident in Fig. 13. This is most likely due to the fact that the ligaments are mainly oriented in the in-plane directions and therefore there would be less resistance to compressive forces to close up the gaps parallel to these ligaments than those normal to them. In addition, curve-fitting correlations between the porosity and each of the through-plane permeability and the in-plane permeability (which represent the impact of compression on the permeability) are shown in Figure S.18 in the supplementary material.

The average through- and in-plane permeability values are almost the same for the uncompressed nickel foam signifying the high isotropy of this material; the anisotropy ratio was calculated as 1.04 with 0% compression ratio (Fig. 14). This value is in good agreement with those reported in the literature for the anisotropy ratio of the nickel foam [113–115]. Interestingly, the anisotropic ratio starts to increase to around 1.48 with 20% compression ratio and to around 1.82 with 40% compression ratio. As mentioned earlier, this is due to the gas permeability being more sensitive to the compression in the in-plane direction than the through-plane direction. Therefore, when using nickel foam as GDLs, the validity of the assumption that the nickel foam GDL is isotropic in the PEFC models needs to be carefully examined.

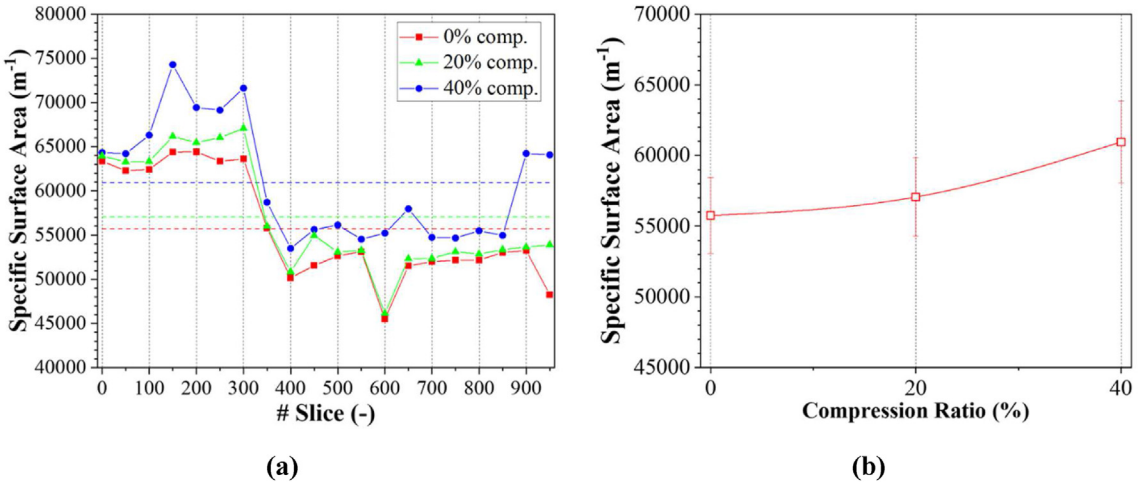

Fig. 12 – (a) Specific surface area values for the uncompressed, 20% compressed, and 40% compressed CT nickel foam slices and (b) the mean specific surface area as a function of the compression ratio. Note that the error bars represent 95% confidence intervals.

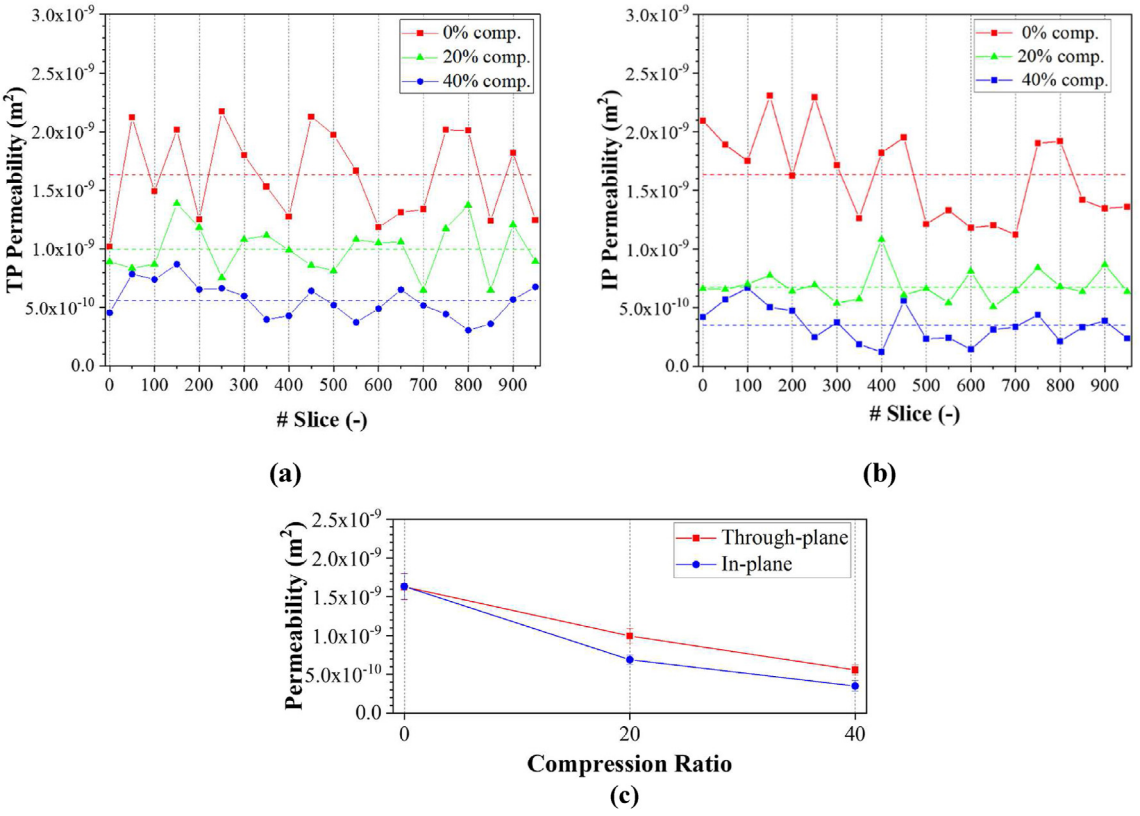

Fig. 13 – (a) Through-plane and (b) in-plane permeability values and (c) the mean permeability values for the uncompressed, 20%, and 40% compressed CT nickel foam slices. Note that the error bars represent 95% confidence intervals. Note that the error bars represent 95% confidence intervals.

Effective diffusivity

The effective diffusivity of oxygen into nitrogen in both the through- and in-plane directions were computationally estimated for all the 20 CT nickel foam slices; see Fig. 15. The mean effective diffusivity values in the through- and in-plane directions for the uncompressed nickel foam are 0.161 and 0.170 cm^2/s, respectively. As with the permeability, the effective diffusivity is expected to decrease with compression. The through-plane and the in-plane effective diffusivity values become 0.152 and 0.154 cm^2/s with 20% compression ratio, and 0.145 and 0.143 cm^2/s with 40% compression ratio. These effective diffusivity values are notably higher than those of the conventional carbon fibres based GDLs. For

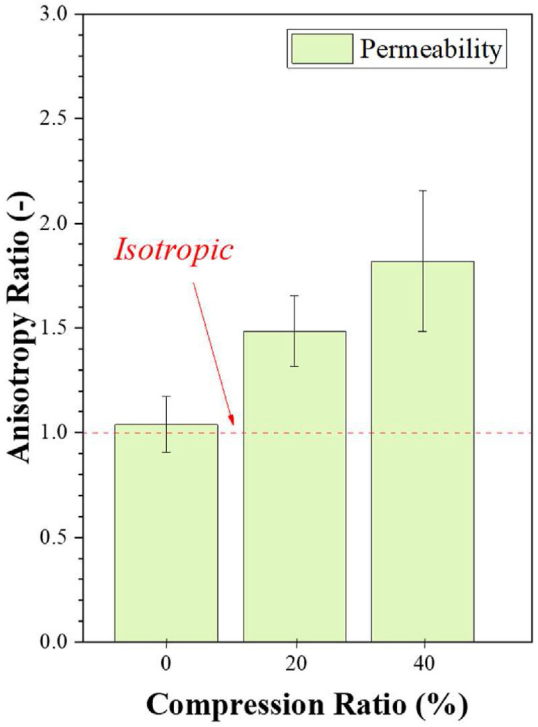

Fig. 14 – The anisotropy ratios of the gas permeability of nickel foam under different compression ratios. Note that the error bars represent 95% confidence intervals.

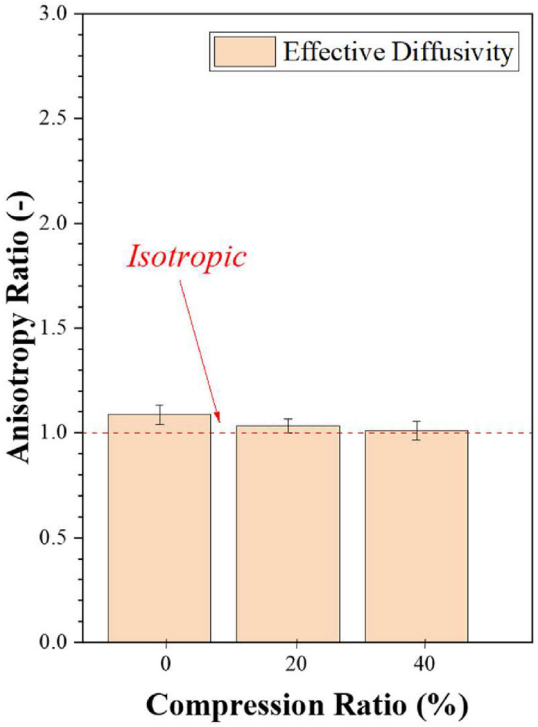

Fig. 16 – The anisotropy ratios of the effective diffusivity of nickel foam under different compression ratios. Note that the error bars represent 95% confidence intervals.

example, the through-plane effective diffusivity for the uncoated SGL GDL was reported to be between 0.153 and 0.08 cm^2/s and for Toray GDL to be between 0.081 and 0.033 cm^2/s [75,116]. Similarly, the in-plane effective diffusivity of Toray GDL was found to vary between 0.78 and 0.02 cm^2/s. It should be noted that the above lower limits are for the compressed GDLs while the upper limits are for the uncompressed GDLs. Unlike the gas permeability of compressed nickel foam, the effective diffusivity of the nickel foam was found to be highly isotropic even with high compression ratios. Namely, the anisotropic ratio of the effective diffusivity is 1.05 with 0% compression ratio, 1.03 with 20% compression ratio and 1.01 with 40% compression ratio; see Fig. 16. Furthermore, curve-fitting correlations between the porosity and each of the through-plane effective diffusivity and the in-plane effective diffusivity (representing the impact of compression on the effective diffusivity) are exhibited in Figure S.19 in the supplementary material.

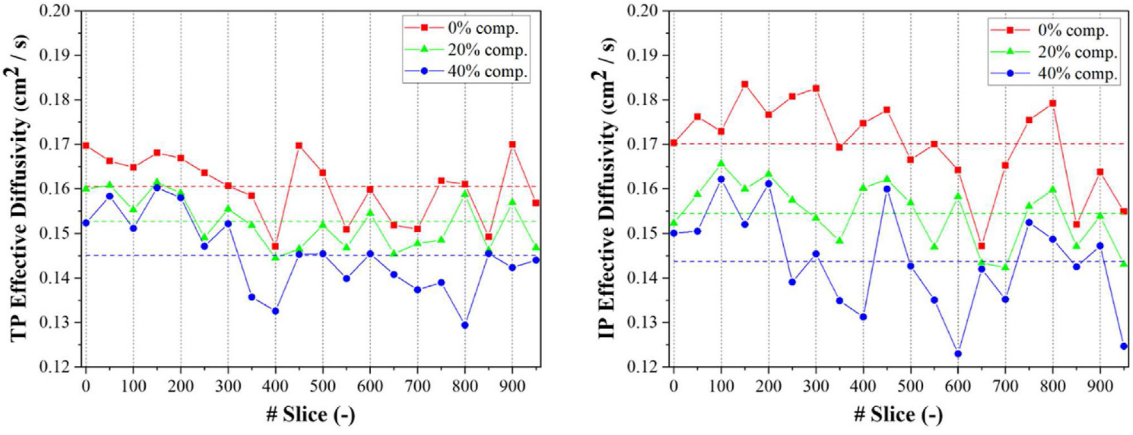

Fig. 15 – (a) The through-plane and (b) the in-plane effective diffusivity values for the uncompressed, 20% compressed, and 40% CT nickel foam slices.

Conclusions

Nickel foam is a serious candidate for gas diffusion layers in polymer electrolyte fuel cells and this is due to their superior structural and transport properties. In this work, the impact of realistic compression (mimicking those applied to the PEFCs) on some of the key structural and transport properties has been investigated using computationally efficient two-dimensional X-ray CT based images and numerical models. These investigated structural and transport properties are: porosity, tortuosity, pore size distribution, ligament thickness distribution, and specific surface area, gas permeability and effective diffusivity. The following are the main findings of the study.

- The porosity of nickel foam was found to decrease slightly with realistic compressions. Namely, the mean porosity of nickel foam (~0.89) decreased by less 6% (0.84) when compressed by 40%. These values are higher than those demonstrated by the conventional carbon substrates under similar compressions; this implies less mass transport resistance when using nickel foam as GDLs.
- The pore size was shown to considerably decrease with compression; the mean pore size of nickel foam (~175 μm) decreased by around 60% (71 μm) when nickel foam was compressed by 40%. Interestingly, the ligament thickness was found to decrease by around 10% when compressing nickel foam by 40%; the ligament thickness decreased from ~100 μm to ~90 μm with 40% compression ratio and this is due to the fact that the ligaments encapsulate some small pores. On the other hand, the specific surface area was shown to increase with compression; it increases from 55700 m^{-1} (uncompressed nickel foam) to 61000 m^{-1} with 40% compression ratio.
- The in-plane tortuosity of nickel foam increases with compression; it increased from ~1.14 to 1.19 with 40% compression ratio. On the other hand, its through-plane tortuosity (~1.18) was found to increase with 20% compression (~1.20) and then decrease (~1.18) with 40% compression. This is most likely due to the observation that the ligaments are mainly oriented in the in-plane directions and therefore the pores parallel to these ligaments are closed up with compression; thus, creating more in-plane tortuous flow paths. However, a compression beyond a certain value appear to straighten the pathways in the through-plane directions.
- The gas permeability of nickel foam significantly decreases with compression particularly in the in-plane direction; the mean through-plane permeability (1.63×10^{-9} m^2) decreased by around 65% (5.57×10^{-10} m^2) and mean the in-plane permeability (1.64×10^{-9} m^2) by around 80% (3.51×10^{-10} m^2) with 40% compression ratio. The numbers show that gas permeability of the uncompressed nickel foam is highly isotropic; the anisotropic ratio (which is the ratio between the through-plane and in-plane gas permeability) is around unity. However, this factor increases significantly with compression; it increased to around 1.5 with 20% compression ratio and to around 1.8 with 40% compression ratio. This is mainly due to the ligaments being mainly oriented in the in-plane direction, thus allowing for easier closing up of the gaps between them compared to those normal to the ligaments.
- Unlike gas permeability, the effective diffusivity of oxygen into nitrogen was found to be highly isotropic and less sensitive to compression. Namely, the through-plane effective diffusivity (0.161 cm^2/s) decreased by around 10% (0.145 cm^2/s) and the in-plane effective diffusivity (0.170 cm^2/s) decreased by around 15% (0.143 cm^2/s) with 40% compression ratio. Interestingly, the isotropy of the effective diffusivity was found to slightly decrease with compression; the anisotropic ratio decreased from 1.05 to 1.01 with 40% compression ratio.
- The data generated form this study for the structural and the mass transport properties of the nickel foam-based GDL under realistic mechanical compressions are valuable for the PEFC models. Namely, they could be fed into these models to improve the accuracy and the reliability of their predictions. This is an exciting topic for a future work.

Declaration of competing interest

The authors declare that they have no known competing financial interests or personal relationships that could have appeared to influence the work reported in this paper.

Acknowledgements

The first author, Mustafa Ercelik, would like to thank the Republic of Turkey Ministry of National Education for funding his studentship at the University of Sheffield.

Appendix A. Supplementary data

Supplementary data to this article can be found online at https://doi.org/10.1016/j.ijhydene.2023.07.001.

Nomenclature

Symbols

C	Concentration (mol/m^3)
ΔC	Concentration difference (mol/m^3)
D	Diffusion coefficient (cm^2/s)
D_{O2}	Bulk oxygen diffusivity into nitrogen (cm^2/s)
D_{ij}^{eff}	Effective diffusivity of the species *i* into species *j* (cm^2/s)
I	Identity matrix
J	Molar flux ($mol/(m^2\text{-}s)$)
K	Permeability (m^2)
L	Length (mm)
P	Pressure (Pa)
ΔP	Pressure difference (Pa)
R	Sink source
u	Fluid velocity (m/s)

u_{mag}	Velocity magnitude (m/s)
u_x	Velocity in through-plane direction (m/s)
u_y	Velocity in in-plane direction (m/s)
X_{comp}	Compression ratio (–)

Greek symbols

ε	Porosity (–)
μ	Dynamic Viscosity of fluid (Pa·s)
ρ	Fluid density (kg/m^3)
τ	Tortuosity (–)

Abbreviations

BET	Brunauer–Emmett–Teller
CT	Computed tomography
FFP	Flow field plate
GDL	Gas diffusion layer
MIP	Mercury intrusion porosimetry
ORR	Oxygen reduction reaction
PEFC	Polymer electrolyte fuel cell
SEM	Scanning electron microscopy
SSA	Specific surface area (m^{-1})

Subscripts & superscripts

ave	Average
comp	Compression
eff	Effective
exp	Experimental
i,j	the species i into species j
in	Inlet
IP	In-plane
mag	Magnitude
out	Outlet
O_2	Oxygen
TP	Through-plane
x	x-direction
y	y-direction

REFERENCES

[1] Ozden A, Shahgaldi S, Li X, Hamdullahpur F. A review of gas diffusion layers for proton exchange membrane fuel cells—with a focus on characteristics, characterization techniques, materials and designs. Prog Energy Combust Sci 2019;74:50–102. https://doi.org/10.1016/j.pecs.2019.05.002.

[2] Pang Y, Hao L, Wang Y. Convolutional neural network analysis of radiography images for rapid water quantification in PEM fuel cell. Appl Energy 2022;321:119352. https://doi.org/10.1016/j.apenergy.2022.119352.

[3] Kahveci EE, Taymaz I. Assessment of single-serpentine PEM fuel cell model developed by computational fluid dynamics. Fuel 2018;217:51–8. https://doi.org/10.1016/j.fuel.2017.12.073.

[4] Kahveci EE, Taymaz I. Experimental study on performance evaluation of PEM fuel cell by coating bipolar plate with materials having different contact angle. Fuel 2019;253:1274–81. https://doi.org/10.1016/j.fuel.2019.05.110.

[5] Zhao J, Tu Z, Chan SH. Carbon corrosion mechanism and mitigation strategies in a proton exchange membrane fuel cell (PEMFC): a review. J Power Sources 2021;488. https://doi.org/10.1016/j.jpowsour.2020.229434.

[6] Zhang M, Yu M, Liu Z, Tu Z, Liu W. Moisture migration in the cathode GDL of PEMFC under variable physical parameters based on a modified two-fluid model. Int J Hydrogen Energy 2023;48:15657–76. https://doi.org/10.1016/j.ijhydene.2023.01.055.

[7] Wang Y, Ruiz Diaz DF, Chen KS, Wang Z, Adroher XC. Materials, technological status, and fundamentals of PEM fuel cells – a review. Mater Today 2020;32:178–203. https://doi.org/10.1016/j.mattod.2019.06.005.

[8] Arvay A, Yli-Rantala E, Liu CH, Peng XH, Koski P, Cindrella L, et al. Characterization techniques for gas diffusion layers for proton exchange membrane fuel cells - a review. J Power Sources 2012;213:317–37. https://doi.org/10.1016/j.jpowsour.2012.04.026.

[9] Lee S, Tam J, Li W, Yu B, Cho HJ, Samei J, et al. Multi-scale morphological characterization of Ni foams with directional pores. Mater Char 2019;158. https://doi.org/10.1016/j.matchar.2019.109939.

[10] Meyer Q, Liu S, Ching K, Da Y, Zhao C. Operando monitoring of the evolution of triple-phase boundaries in proton exchange membrane fuel cells. J Power Sources 2023;557:232539. https://doi.org/10.1016/j.jpowsour.2022.232539.

[11] Alaefour I, Shahgaldi S, Ozden A, Li X, Hamdullahpur F. The role of flow-field layout on the conditioning of a proton exchange membrane fuel cell. Fuel 2018;230:98–103. https://doi.org/10.1016/j.fuel.2018.05.062.

[12] Thanasilp S, Hunsom M. Effect of MEA fabrication techniques on the cell performance of Pt-Pd/C electrocatalyst for oxygen reduction in PEM fuel cell. Fuel 2010;89:3847–52. https://doi.org/10.1016/j.fuel.2010.07.008.

[13] Wilberforce T, El-Hassan Z, Khatib FN, Al Makky A, Baroutaji A, Carton JG, et al. Developments of electric cars and fuel cell hydrogen electric cars. Int J Hydrogen Energy 2017;42:25695–734. https://doi.org/10.1016/j.ijhydene.2017.07.054.

[14] Das HS, Tan CW, Yatim AHM. Fuel cell hybrid electric vehicles: a review on power conditioning units and topologies. Renew Sustain Energy Rev 2017;76:268–91. https://doi.org/10.1016/j.rser.2017.03.056.

[15] Chen X, Liu B, Sun C, Xia X. Effects of microscopic morphology of ligament and porous parameter on spectral radiative properties of nickel foams. Infrared Phys Technol 2022;123:104208. https://doi.org/10.1016/j.infrared.2022.104208.

[16] Taner T. The novel and innovative design with using H2 fuel of PEM fuel cell: efficiency of thermodynamic analyze. Fuel 2021;302:121109. https://doi.org/10.1016/j.fuel.2021.121109.

[17] Bahari M, Rostami M, Entezari A, Ghahremani S, Etminan M. Performance evaluation and multi-objective optimization of a novel UAV propulsion system based on PEM fuel cell. Fuel 2022;311:122554. https://doi.org/10.1016/j.fuel.2021.122554.

[18] Wan Z, Yan H, Sun Y, Yang C, Chen X, Kong X, et al. Thermal management improvement of air-cooled proton exchange membrane fuel cell by using metal foam flow field. Appl Energy 2023;333:120642. https://doi.org/10.1016/j.apenergy.2023.120642.

[19] Ozden A, Shahgaldi S, Zhao J, Li X, Hamdullahpur F. Assessment of graphene as an alternative microporous layer material for proton exchange membrane fuel cells. Fuel 2018;215:726–34. https://doi.org/10.1016/j.fuel.2017.11.109.

[20] Ozden A, Alaefour IE, Shahgaldi S, Li X, Colpan CO, Hamdullahpur F. Gas diffusion layers for PEM fuel cells: ex- and in-situ characterization. Elsevier; 2018. https://doi.org/10.1016/B978-0-12-813734-5.00040-8.

[21] Sánchez M, Pierna AR, Lorenzo A, Del Val JJ. Effect of cocatalyst and composition on catalytic performance of amorphous alloys for ethanol electrooxidation and PEMFCs.

Int J Hydrogen Energy 2016;41:19749. https://doi.org/10.1016/j.ijhydene.2016.06.064. –55.
[22] El-Kharouf A, Mason TJ, Brett DJL, Pollet BG. Ex-situ characterisation of gas diffusion layers for proton exchange membrane fuel cells. J Power Sources 2012;218:393–404. https://doi.org/10.1016/j.jpowsour.2012.06.099.
[23] Aldakheel F, Ismail MS, Hughes KJ, Ingham DB, Ma L, Pourkashanian M. Effects of compression on mechanical integrity, gas permeability and thermal stability of gas diffusion layers with/without sealing gaskets. Int J Hydrogen Energy 2021;46:22907–19. https://doi.org/10.1016/j.ijhydene.2021.04.087.
[24] Ismail MS, Damjanovic T, Ingham DB, Pourkashanian M, Westwood A. Effect of polytetrafluoroethylene-treatment and microporous layer-coating on the electrical conductivity of gas diffusion layers used in proton exchange membrane fuel cells. J Power Sources 2010;195:2700–8. https://doi.org/10.1016/j.jpowsour.2009.11.069.
[25] Ismail MS, Damjanovic T, Hughes K, Ingham DB, Ma L, Pourkashanian M, et al. Through-plane permeability for untreated and PTFE-treated gas diffusion layers in proton exchange membrane fuel cells. J Fuel Cell Sci Technol 2010;7:0510161. https://doi.org/10.1115/1.4000685. –7.
[26] Ismail MS, Hassanpour A, Ingham DB, Ma L, Pourkashanian M. On the compressibility of gas diffusion layers in proton exchange membrane fuel cells. Fuel Cell 2012;12:391–7. https://doi.org/10.1002/fuce.201100054.
[27] Okereke IC, Ismail MS, Ingham D, Hughes KJ, Ma L, Pourkashanian M. The effects of GDL anisotropic transport properties on the PEFC performance. Int J Numer Methods Heat Fluid Flow 2022. https://doi.org/10.1108/hff-05-2022-0284.
[28] Park S, Popov BN. Effect of a GDL based on carbon paper or carbon cloth on PEM fuel cell performance. Fuel 2011;90:436–40. https://doi.org/10.1016/j.fuel.2010.09.003.
[29] Turkmen AC, Celik C. The effect of different gas diffusion layer porosity on proton exchange membrane fuel cells. Fuel 2018;222:465–74. https://doi.org/10.1016/j.fuel.2018.02.058.
[30] Jayakumar A, Sethu SP, Ramos M, Robertson J, Al-Jumaily A. A technical review on gas diffusion, mechanism and medium of PEM fuel cell. Ionics 2015;21:1–18. https://doi.org/10.1007/s11581-014-1322-x.
[31] Ismail MS, Borman D, Damjanovic T, Ingham DB, Pourkashanian M. On the through-plane permeability of microporous layer-coated gas diffusion layers used in proton exchange membrane fuel cells. Int J Hydrogen Energy 2011;36:10392–402. https://doi.org/10.1016/j.ijhydene.2010.09.012.
[32] Ye L, Qiu D, Peng L, Lai X. Microstructures and electrical conductivity properties of compressed gas diffusion layers using X-ray tomography. Appl Energy 2022;326:119934. https://doi.org/10.1016/j.apenergy.2022.119934.
[33] Zhao J, Shahgaldi S, Ozden A, Alaefour IE, Li X, Hamdullahpur F. Effect of catalyst deposition on electrode structure, mass transport and performance of polymer electrolyte membrane fuel cells. Appl Energy 2019;255:113802. https://doi.org/10.1016/j.apenergy.2019.113802.
[34] Park J, Oh H, Ha T, Lee Y Il, Min K. A review of the gas diffusion layer in proton exchange membrane fuel cells: durability and degradation. Appl Energy 2015;155:866–80. https://doi.org/10.1016/j.apenergy.2015.06.068.
[35] Pan Y, Wang H, Brandon NP. Gas diffusion layer degradation in proton exchange membrane fuel cells: mechanisms, characterization techniques and modelling approaches. J Power Sources 2021;513:230560. https://doi.org/10.1016/j.jpowsour.2021.230560.
[36] Ozden A, Shahgaldi S, Zhao J, Li X, Hamdullahpur F. Degradations in porous components of a proton exchange membrane fuel cell under freeze-thaw cycles: morphology and microstructure effects. Int J Hydrogen Energy 2020;45:3618–31. https://doi.org/10.1016/j.ijhydene.2018.10.209.
[37] Bose AB, Zhu X. Design of stable and durable polymer electrolyte membrane fuel cells by embedding hydrophobic cage-structured material in cell components. Fuel 2019;235:954–61. https://doi.org/10.1016/j.fuel.2018.08.051.
[38] Shen J, Xu L, Chang H, Tu Z, Chan SH. Partial flooding and its effect on the performance of a proton exchange membrane fuel cell. Energy Convers Manag 2020;207:112537. https://doi.org/10.1016/j.enconman.2020.112537.
[39] El-kharouf A, Pollet BG. Gas diffusion media and their degradation. Elsevier Inc.; 2012. https://doi.org/10.1016/B978-0-12-386936-4.10004-1.
[40] Bosomoiu M, Tsotridis G, Bednarek T. Study of effective transport properties of fresh and aged gas diffusion layers. J Power Sources 2015;285:568–79. https://doi.org/10.1016/j.jpowsour.2015.03.132.
[41] Nitta I, Hottinen T, Himanen O, Mikkola M. Inhomogeneous compression of PEMFC gas diffusion layer. Part I. Experimental. J Power Sources 2007;171:26–36. https://doi.org/10.1016/j.jpowsour.2006.11.018.
[42] Ozden A, Shahgaldi S, Li X, Hamdullahpur F. The impact of ionomer type on the morphological and microstructural degradations of proton exchange membrane fuel cell electrodes under freeze-thaw cycles. Appl Energy 2019;238:1048–59. https://doi.org/10.1016/j.apenergy.2019.01.136.
[43] Yan X, Lin C, Zheng Z, Chen J, Wei G, Zhang J. Effect of clamping pressure on liquid-cooled PEMFC stack performance considering inhomogeneous gas diffusion layer compression. Appl Energy 2020;258:114073. https://doi.org/10.1016/j.apenergy.2019.114073.
[44] Tan WC, Saw LH, Thiam HS, Xuan J, Cai Z, Yew MC. Overview of porous media/metal foam application in fuel cells and solar power systems. Renew Sustain Energy Rev 2018;96:181–97. https://doi.org/10.1016/j.rser.2018.07.032.
[45] Bonnet JP, Topin F, Tadrist L. Flow laws in metal foams: compressibility and pore size effects. Transport Porous Media 2008;73:233–54. https://doi.org/10.1007/s11242-007-9169-5.
[46] Awin Y, Dukhan N. Experimental performance assessment of metal-foam flow fields for proton exchange membrane fuel cells. Appl Energy 2019;252:113458. https://doi.org/10.1016/j.apenergy.2019.113458.
[47] Zhang G, Bao Z, Xie B, Wang Y, Jiao K. Three-dimensional multi-phase simulation of PEM fuel cell considering the full morphology of metal foam flow field. Int J Hydrogen Energy 2021;46:2978–89. https://doi.org/10.1016/j.ijhydene.2020.05.263.
[48] Tseng CJ, Tsai BT, Liu ZS, Cheng TC, Chang WC, Lo SK. A PEM fuel cell with metal foam as flow distributor. Energy Convers Manag 2012;62:14–21. https://doi.org/10.1016/j.enconman.2012.03.018.
[49] Tsai BT, Tseng CJ, Liu ZS, Wang CH, Lee CI, Yang CC, et al. Effects of flow field design on the performance of a PEM fuel cell with metal foam as the flow distributor. Int J Hydrogen Energy 2012;37:13060–6. https://doi.org/10.1016/j.ijhydene.2012.05.008.
[50] Baroutaji A, Carton JG, Stokes J, Olabi AG. Application of open pore cellular foam for air breathing PEM fuel cell. Int J

Hydrogen Energy 2017;42:25630–8. https://doi.org/10.1016/j.ijhydene.2017.05.114.
[51] Shin DK, Yoo JH, Kang DG, Kim MS. Effect of cell size in metal foam inserted to the air channel of polymer electrolyte membrane fuel cell for high performance. Renew Energy 2018;115:663–75. https://doi.org/10.1016/j.renene.2017.08.085.
[52] Zheng W, Liu M, Lee LYS. Best practices in using foam-type electrodes for electrocatalytic performance benchmark. ACS Energy Lett 2020;5:3260–4. https://doi.org/10.1021/acsenergylett.0c01958.
[53] Liu R, Zhou W, Li S, Li F, Ling W. Performance improvement of proton exchange membrane fuel cells with compressed nickel foam as flow field structure. Int J Hydrogen Energy 2020;45:17833–43. https://doi.org/10.1016/j.ijhydene.2020.04.238.
[54] Tabe Y, Nasu T, Morioka S, Chikahisa T. Performance characteristics and internal phenomena of polymer electrolyte membrane fuel cell with porous flow field. J Power Sources 2013;238:21–8. https://doi.org/10.1016/j.jpowsour.2013.03.047.
[55] Chen X, Yang C, Sun Y, Liu Q, Wan Z, Kong X, et al. Water management and structure optimization study of nickel metal foam as flow distributors in proton exchange membrane fuel cell. Appl Energy 2022;309:118448. https://doi.org/10.1016/j.apenergy.2021.118448.
[56] Zamel N, Li X. Effective transport properties for polymer electrolyte membrane fuel cells - with a focus on the gas diffusion layer. Prog Energy Combust Sci 2013;39:111–46. https://doi.org/10.1016/j.pecs.2012.07.002.
[57] Jankovic J, Zhang S, Putz A, Saha MS, Susac D. Multiscale imaging and transport modeling for fuel cell electrodes. J Mater Res 2019;34:579–91. https://doi.org/10.1557/jmr.2018.458.
[58] Rosén T, Eller J, Kang J, Prasianakis NI, Mantzaras J, Büchi FN. Saturation dependent effective transport properties of PEFC gas diffusion layers. J Electrochem Soc 2012;159:F536–44. https://doi.org/10.1149/2.005209jes.
[59] Bao Z, Li Y, Zhou X, Gao F, Du Q, Jiao K. Transport properties of gas diffusion layer of proton exchange membrane fuel cells: effects of compression. Int J Heat Mass Tran 2021;178:121608. https://doi.org/10.1016/j.ijheatmasstransfer.2021.121608.
[60] Gostick JT, Fowler MW, Pritzker MD, Ioannidis MA, Behra LM. In-plane and through-plane gas permeability of carbon fiber electrode backing layers. J Power Sources 2006;162:228–38. https://doi.org/10.1016/j.jpowsour.2006.06.096.
[61] García-Salaberri PA, Zenyuk IV, Shum AD, Hwang G, Vera M, Weber AZ, et al. Analysis of representative elementary volume and through-plane regional characteristics of carbon-fiber papers: diffusivity, permeability and electrical/thermal conductivity. Int J Heat Mass Tran 2018;127:687–703. https://doi.org/10.1016/j.ijheatmasstransfer.2018.07.030.
[62] Fishman Z, Hinebaugh J, Bazylak A. Microscale tomography investigations of heterogeneous porosity distributions of PEMFC GDLs. J Electrochem Soc 2010;157:1643–50. https://doi.org/10.1149/1.3481443.
[63] Obermaier M, Bauer A, Dalkilic M, Rauber M, Scheu C. Gas diffusion layer wettability determination by cyclic voltammetry for automotive fuel cells. Fuel Cell 2021:221–33. https://doi.org/10.1002/fuce.202000184.
[64] Kaushal S, Sahu AK, Rani M, Dhakate SR. Multiwall carbon nanotubes tailored porous carbon fiber paper-based gas diffusion layer performance in polymer electrolyte membrane fuel cell. Renew Energy 2019;142:604–11. https://doi.org/10.1016/j.renene.2019.04.096.
[65] Vásárhelyi L, Kónya Z, Kukovecz Vajtai R. Microcomputed tomography–based characterization of advanced materials: a review. Mater Today Adv 2020;8:1–13. https://doi.org/10.1016/j.mtadv.2020.100084.
[66] De Chiffre L, Carmignato S, Kruth JP, Schmitt R, Weckenmann A. Industrial applications of computed tomography. CIRP Ann - Manuf Technol 2014;63:655–77. https://doi.org/10.1016/j.cirp.2014.05.011.
[67] Kou X, Sen Li X, Wang Y, Zhang Y, Chen ZY. Distribution and reformation characteristics of gas hydrate during hydrate dissociation by thermal stimulation and depressurization methods. Appl Energy 2020;277:115575. https://doi.org/10.1016/j.apenergy.2020.115575.
[68] Fishman Z, Bazylak A. Heterogeneous through-plane porosity distributions for treated PEMFC GDLs I. PTFE effect. J Electrochem Soc 2011;158:B841. https://doi.org/10.1149/1.3594578.
[69] Fishman Z, Bazylak A. Heterogeneous through-plane porosity distributions for treated PEMFC GDLs. II. Effect of MPL cracks. J Electrochem Soc 2011;158:B846. https://doi.org/10.1149/1.3594636.
[70] Banerjee R, Hinebaugh J, Liu H, Yip R, Ge N, Bazylak A. Heterogeneous porosity distributions of polymer electrolyte membrane fuel cell gas diffusion layer materials with rib-channel compression. Int J Hydrogen Energy 2016;41:14885–96. https://doi.org/10.1016/j.ijhydene.2016.06.147.
[71] Meyer Q, Ashton S, Boillat P, Cochet M, Engebretsen E, Finegan DP, et al. Effect of gas diffusion layer properties on water distribution across air-cooled, open-cathode polymer electrolyte fuel cells: a combined ex-situ X-ray tomography and in-operando neutron imaging study. Electrochim Acta 2016;211:478–87. https://doi.org/10.1016/j.electacta.2016.06.068.
[72] Meyer Q, Mansor N, Iacoviello F, Cullen PL, Jervis R, Finegan D, et al. Investigation of hot pressed polymer electrolyte fuel cell assemblies via X-ray computed tomography. Electrochim Acta 2017;242:125–36. https://doi.org/10.1016/j.electacta.2017.05.028.
[73] Holzer L, Pecho O, Schumacher J, Marmet P, Stenzel O, Büchi FN, et al. Microstructure-property relationships in a gas diffusion layer (GDL) for Polymer Electrolyte Fuel Cells, Part I: effect of compression and anisotropy of dry GDL. Electrochim Acta 2017;227:419–34. https://doi.org/10.1016/j.electacta.2017.01.030.
[74] Ma J, Zhang X, Jiang Z, Ostadi H, Jiang K, Chen R. Flow properties of an intact MPL from nano-tomography and pore network modelling. Fuel 2014;136:307–15. https://doi.org/10.1016/j.fuel.2014.07.040.
[75] Zenyuk IV, Parkinson DY, Connolly LG, Weber AZ. Gas-diffusion-layer structural properties under compression via X-ray tomography. J Power Sources 2016;328:364–76. https://doi.org/10.1016/j.jpowsour.2016.08.020.
[76] Je J, Doh S, Kim J, Kim MH. Heterogeneous porosity distribution under compression of gas diffusion layer using synchrotron X-ray tomography. ECS Meet Abstr 2012;MA2012–02:1494. https://doi.org/10.1149/ma2012-02/13/1494. –1494.
[77] Fly A, Meyer Q, Whiteley M, Iacoviello F, Neville T, Shearing PR, et al. X-ray tomography and modelling study on the mechanical behaviour and performance of metal foam flow-fields for polymer electrolyte fuel cells. Int J Hydrogen Energy 2019;44:7583–95. https://doi.org/10.1016/j.ijhydene.2019.01.206.
[78] Wu Y, Lu X, Cho JIS, Rasha L, Whiteley M, Neville TP, et al. Multi-length scale characterization of compression on metal foam flow-field based fuel cells using X-ray computed tomography and neutron radiography. Energy Convers

Manag 2021;230:1–10. https://doi.org/10.1016/j.enconman.2020.113785.
[79] Ercelik M, Ismail MS, Ingham DB, Hughes KJ, Ma L. Efficient X-ray CT-based numerical computations of structural and mass transport properties of nickel foam-based GDLs for PEFCs. Energy 2023;262:125531. https://doi.org/10.1016/j.energy.2022.125531.
[80] Tamayol A, McGregor F, Bahrami M. Single phase through-plane permeability of carbon paper gas diffusion layers. J Power Sources 2012;204:94–9. https://doi.org/10.1016/j.jpowsour.2011.11.084.
[81] Poserin V, Marcuson S, Shu J, Wilkinson DS. CVD technique for Inco nickel foam production. Adv Eng Mater 2004;6:454–9. https://doi.org/10.1002/adem.200405142.
[82] Kia A, Wong HS, Cheeseman CR. Clogging in permeable concrete: a review. J Environ Manag 2017;193:221–33. https://doi.org/10.1016/j.jenvman.2017.02.018.
[83] Nabovati A, Hinebaugh J, Bazylak A, Amon CH. Effect of porosity heterogeneity on the permeability and tortuosity of gas diffusion layers in polymer electrolyte membrane fuel cells. J Power Sources 2014;248:83–90. https://doi.org/10.1016/j.jpowsour.2013.09.061.
[84] ImageJ/Fiji. https://imagej.net/software/fiji/n.d.
[85] Huo S, Shi WY, Wang RF, Lu BB, Wang Y, Jiao K, et al. Elucidating the operating behavior of PEM fuel cell with nickel foam as cathode flow field. Sci China Technol Sci 2021;64:1041–56. https://doi.org/10.1007/s11431-020-1767-5.
[86] Duan DL, Zhang RL, Ding XJ, Li S. Calculation of specific surface area of foam metals using dodecahedron model. Mater Sci Technol 2006;22:1364–8. https://doi.org/10.1179/174328406X111138.
[87] Oun H, Kennedy A. Experimental investigation of pressure-drop characteristics across multi-layer porous metal structures. J Porous Mater 2014;21:1133–41. https://doi.org/10.1007/s10934-014-9863-y.
[88] Han M, Xu JH, Chan SH, Jiang SP. Characterization of gas diffusion layers for PEMFC. Electrochim Acta 2008;53:5361–7. https://doi.org/10.1016/j.electacta.2008.02.057.
[89] Ahmed DH, Sung HJ, Bae J. Effect of GDL permeability on water and thermal management in PEMFCs-I. Isotropic and anisotropic permeability. Int J Hydrogen Energy 2008;33:3767–85. https://doi.org/10.1016/j.ijhydene.2008.04.024.
[90] Ahmed DH, Sung HJ, Bae J. Effect of GDL permeability on water and thermal management in PEMFCs-II. Clamping force. Int J Hydrogen Energy 2008;33:3786–800. https://doi.org/10.1016/j.ijhydene.2008.04.023.
[91] Lee FC, Ismail MS, Ingham DB, Hughes KJ, Ma L, Lyth SM, et al. Alternative architectures and materials for PEMFC gas diffusion layers: a review and outlook. Renew Sustain Energy Rev 2022;166:112640. https://doi.org/10.1016/j.rser.2022.112640.
[92] Ismail MS, Hughes KJ, Ingham DB, Ma L, Pourkashanian M. Effects of anisotropic permeability and electrical conductivity of gas diffusion layers on the performance of proton exchange membrane fuel cells. Appl Energy 2012;95:50–63. https://doi.org/10.1016/j.apenergy.2012.02.003.
[93] Neehall ND, Ismail MS, Hughes KJ, Pourkashanian M. Effect of composition and structure of gas diffusion layer and microporous layer on the through-plane gas permeability of PEFC porous media. Int J Energy Res 2021;45:20988–1005. https://doi.org/10.1002/er.7158.
[94] Holman JP. Heat transfer. 10th ed. McGraw-Hill; 2010.
[95] Ismail MS, Ingham DB, Hughes KJ, Ma L, Pourkashanian M. Effective diffusivity of polymer electrolyte fuel cell gas diffusion layers: an overview and numerical study. Int J Hydrogen Energy 2015;40:10994–1010. https://doi.org/10.1016/j.ijhydene.2015.06.073.
[96] Orogbemi OM, Ingham DB, Ismail MS, Hughes KJ, Ma L, Pourkashanian M. The effects of the composition of microporous layers on the permeability of gas diffusion layers used in polymer electrolyte fuel cells. Int J Hydrogen Energy 2016;41:21345–51. https://doi.org/10.1016/j.ijhydene.2016.09.160.
[97] Vicente J, Topin F, Daurelle JV. Open celled material structural properties measurement: from morphology to transport properties. Mater Trans 2006;47:2195–202. https://doi.org/10.2320/matertrans.47.2195.
[98] Khayargoli P, Loya V, Lefebvre LP, Medraj M. The impact of microstructure on the permeability of metal foams. CSME 2004 Forum 2004;2004:220–8.
[99] Langlois S, Coeuret F. Flow-through and flow-by porous electrodes of nickel foam. I. Material characterization. J Appl Electrochem 1989;19:43–50. https://doi.org/10.1007/BF01039388.
[100] Brun E, Vicente J, Topin F, Occelli R. Geometrical measurement of real foams from 3D images. MetFoam 2007 - Proc 5th Int Conf Porous Met Met Foam 2008:425. –8.
[101] Miwa S, Revankar ST. Hydrodynamic characterization of nickel metal foameffects of pore structure and permeability. Heat Tran Eng 2012;33:800–8. https://doi.org/10.1080/01457632.2012.646872.
[102] Milazzo RG, Privitera SMS, Scalese S, Lombardo SA. Effect of morphology and mechanical stability of nanometric platinum layer on nickel foam for hydrogen evolution reaction. Energies 2019;12. https://doi.org/10.3390/en12163116.
[103] Dukhan N, Patel P. Equivalent particle diameter and length scale for pressure drop in porous metals. Exp Therm Fluid Sci 2008;32:1059–67. https://doi.org/10.1016/j.expthermflusci.2007.12.001.
[104] Dukhan N. Correlations for the pressure drop for flow through metal foam. Exp Fluid 2006;41:665–72. https://doi.org/10.1007/s00348-006-0194-x.
[105] Boomsma K, Poulikakos D, Zwick F. Metal foams as compact high performance heat exchangers. Mech Mater 2003;35:1161–76. https://doi.org/10.1016/j.mechmat.2003.02.001.
[106] Flitsanov Y, Kribus A. A cooler for dense-array CPV receivers based on metal foam. Sol Energy 2018;160:25–31. https://doi.org/10.1016/j.solener.2017.12.002.
[107] Kang DG, Lee DK, Choi JM, Shin DK, Kim MS. Study on the metal foam flow field with porosity gradient in the polymer electrolyte membrane fuel cell. Renew Energy 2020;156:931–41. https://doi.org/10.1016/j.renene.2020.04.142.
[108] Medraj M, Baril E, Loya V, Lefebvre LP. The effect of microstructure on the permeability of metallic foams. J Mater Sci 2007;42:4372–83. https://doi.org/10.1007/s10853-006-0602-x.
[109] Gerbaux O, Vercueil T, Memponteil A, Bador B. Experimental characterization of single and two-phase flow through nickel foams. Chem Eng Sci 2009;64:4186–95. https://doi.org/10.1016/j.ces.2009.06.056.
[110] Topin F, Bonnet JP, Madani B, Tadrist L. Experimental analysis of multiphase flow in metallic foam: flow laws, heat transfer and convective boiling. Adv Eng Mater 2006;8:890–9. https://doi.org/10.1002/adem.200600102.
[111] Hugo J-M, Brun E, Topi F. Metal foam effective transport properties. Evaporation, condens heat transf. 2011. https://doi.org/10.5772/21321.
[112] Ismail MS, Hughes KJ, Ingham DB, Ma L, Pourkashanian M. Effect of PTFE loading of gas diffusion layers on the performance of proton exchange membrane fuel cells

running at high-efficiency operating conditions. Int J Energy Res 2013;37:1592–9. https://doi.org/10.1002/er.2968.
[113] Banhart J. Manufacture, characterisation and application of cellular metals and metal foams. Prog Mater Sci 2001;46:559–632. https://doi.org/10.1016/S0079-6425(00)00002-5.
[114] Montillet A, Comiti J, Legrand J. Determination of structural parameters of metallic foams from permeametry measurements. J Mater Sci 1992;27:4460–4. https://doi.org/10.1007/BF00541579.
[115] Jadhav PH, Gnanasekaran N, Perumal DA. Numerical consideration of LTNE and Darcy extended forchheimer models for the analysis of forced convection in a horizontal pipe in the presence of metal foam. J Heat Tran 2021;143:1–16. https://doi.org/10.1115/1.4048622.
[116] Becker J, Flückiger R, Reum M, Büchi FN, Marone F, Stampanoni M. Determination of material properties of gas diffusion layers: experiments and simulations using phase contrast tomographic microscopy. J Electrochem Soc 2009;156:B1175. https://doi.org/10.1149/1.3176876.